

UNLOCKING THE FULL POTENTIAL OF EXTRAGALACTIC $\text{Ly}\alpha$ THROUGH ITS POLARIZATION PROPERTIES

MARIUS B. EIDE,¹ MAX GRONKE,^{2,3} MARK DIJKSTRA,² AND MATTHEW HAYES⁴

¹*Max-Planck-Institut für Astrophysik, Karl-Schwarzschild-Straße 1, D-85741 Garching, Germany*

²*Institute of Theoretical Astrophysics, University of Oslo, Postboks 1029, NO-0315 Oslo, Norway*

³*Department of Physics, University of California, Santa Barbara, CA 93106, USA*

⁴*Department of Astronomy, Oskar Klein Centre, Stockholm University, AlbaNova University Centre, SE-106 91 Stockholm, Sweden*

(Received 2017 September 13; Revised 2018 February 27; Accepted 2018 March 7)

Submitted to ApJ

ABSTRACT

Lyman- α ($\text{Ly}\alpha$) is a powerful astrophysical probe. Not only is it ubiquitous at high redshifts, it is also a resonant line, making $\text{Ly}\alpha$ photons scatter. This scattering process depends on the physical conditions of the gas through which $\text{Ly}\alpha$ propagates, and these conditions are imprinted on observables such as the $\text{Ly}\alpha$ spectrum and its surface brightness profile. In this work, we focus on a less-used observable capable of probing any scattering process: polarization. We implement the density matrix formalism of polarization into the Monte Carlo radiative transfer code `tlac`. This allows us to treat it as a quantum mechanical process where single photons develop and lose polarization from scatterings in arbitrary gas geometries. We explore static and expanding ellipsoids, biconical outflows, and clumpy multiphase media. We find that photons become increasingly polarized as they scatter and diffuse into the wings of the line profiles, making scattered $\text{Ly}\alpha$ polarized in general. The degree and orientation of $\text{Ly}\alpha$ polarization depends on the kinematics and distribution of the scattering HI gas. We find that it generally probes spatial or velocity space asymmetries and aligns itself tangentially to the emission source. We show that the mentioned observables, when studied separately, can leave similar signatures for different source models. We conclude by revealing how a joint analysis of the $\text{Ly}\alpha$ spectra, surface brightness profiles, and polarization can break these degeneracies and help us extract unique physical information on galaxies and their environments from their strongest, most prominent emission line.

Keywords: galaxies: high-redshift – galaxies: halo – galaxies: ISM – line: formation – polarization – radiative transfer

1. INTRODUCTION

Lyman- α ($\text{Ly}\alpha$) is the torch that lights up the distant Universe. Partridge & Peebles (1967) recognized $\text{Ly}\alpha$ to be the strongest tracer of recombining ionized hydrogen (HII) in young, (star) forming galaxies. However, the search for redshifted $\text{Ly}\alpha$ emission was fruitless until the late 1980s, when $\text{Ly}\alpha$ finally was found in known radio galaxies (see e.g. Djorgovski et al. 1985; Hu & Cowie 1987 or the overview by Spinrad 1989). Today, $\text{Ly}\alpha$ heralds the presence of the most distant sources known to humankind (e.g. through absorption, Oesch et al. 2016 or emission, Zitrin et al. 2015), and detecting $\text{Ly}\alpha$ has become one of the primary science

goals of future instruments and telescopes that are developed to understand the high- z Universe (see e.g. reviews by Dijkstra 2014 and Hayes 2015).

The question remains what one can learn from observations of $\text{Ly}\alpha$ emission (and/or absorption). Thus far, observational efforts, as well as theoretical advances geared toward $\text{Ly}\alpha$ radiation, have focused primarily on the modulation of *intensity*. However $\text{Ly}\alpha$ radiation (or radiation of any wavelength) possesses two more degrees of freedom¹, which quantify its polarization properties. These are often represented through the Stokes Q and U parameters, and give the direction and degree of polarization. In this work we explore

Corresponding author: Marius Berge Eide
eide@MPA-Garching.MPG.DE

¹ A third degree of freedom also exist for circularly polarized light: the time-dependence of the polarization angle, expressed through Stokes V parameter.

what additional knowledge can be obtained from these observables.

The potential power of Ly α lies in its resonance nature. In contrast to H α , which escapes unobstructed from its production site following recombination, a Ly α photon can undergo a tremendous number of scatterings after creation, where the precise number depends on HI column density, geometry and kinematics (Adams 1972; Dijkstra 2014). Each scattering event results in a slight change in position and frequency. This dual diffusion process (Osterbrock 1962) imprints signatures on the emergent observables, and potentially reveals properties of the scattering medium along the paths that offered least resistance to the photons (see e.g. Dijkstra et al. 2016; Gronke & Dijkstra 2016).

These signatures can also act as keys to uncovering the emission mechanism. Centrally emitted Ly α photons, e.g. when they were created as nebular emission powered by Pop II stars (Chapman et al. 2004), Pop III stars (Schaefer 2002, 2003) or a nuclear black hole² (Geach et al. 2009) must scatter significantly in most cases prior to escape. Spatially extended Ly α emission can be produced by inflowing, cooling gas (Haiman et al. 2000), gas that has been shock heated by supernova explosions (Mori et al. 2004) or by galactic superwinds (Taniguchi & Shioya 2000), or as fluorescent radiation from an external ionizing field (Hogan & Weymann 1987; Cantalupo et al. 2005). These photons do not need to escape from the dense interstellar medium (ISM), and therefore typically scatter less. With Ly α ubiquitously present in galaxies, surveys provide a wealth of observations open for interpretation (e.g. Steidel et al. 2011; Wisotzki et al. 2016; Shibuya et al. 2018; Herenz et al. 2017). Theoretical work exploring the modulation of Ly α observables by radiative transfer effects, aim to convert these observables into constraints on the physical conditions of the gas in and around galaxies.

Currently, two quantities provide the main observables. One is the *spectrum*, which encodes information on the frequency diffusion process of the photons, which leads to broadening and shifting of the spectral line shape (Neufeld 1990; Dijkstra et al. 2006), by an amount which depends on kinematics, geometry and dust content of the scattering medium (e.g. Ahn & Lee 1998; Hansen & Oh 2006; Verhamme et al. 2006; Dijkstra & Loeb 2008; Gronke et al. 2015). These models been successful at reproducing observations (Verhamme et al. 2008; Hashimoto et al. 2015; Karman et al. 2017; Yang et al. 2017), though it still unclear how physically realistic the models are (see e.g. Gronke & Dijkstra 2016; Gronke et al. 2016, 2017).

² Such spectrally hard sources would leave notably large Ly α equivalent widths.

One problem is that widely different models can provide similar spectra. For example: the large majority of emission sources having a Ly α peak that is redshifted with respect to other lines in the system (Kunth et al. 1998; Trainor et al. 2015), something that can be easily explained by Ly α scattering through a galactic outflow (Verhamme et al. 2006; Dijkstra et al. 2006). However, it is known that the intergalactic medium (IGM) can also process away Ly α mainly in the blue part of the intensity spectrum, which can leave an intrinsically symmetric emission line with a net redshift (Dijkstra et al. 2007; Laursen et al. 2011). Dijkstra & Loeb (2008) showed that these different models give rise to different levels of polarization. This illustrates that polarization, when combined with spectroscopy, may tell models apart that otherwise are indistinguishable.

The other quantity, the surface brightness profile, can reveal the spatial diffusion process that Ly α photons undergo, before escaping possibly far from the site of emission. The resulting Ly α nebulae have been detected around many Ly α emitting galaxies (Hayes et al. 2013; Wisotzki et al. 2016), with larger counterparts around many quasars (Cantalupo et al. 2014; Lake et al. 2015; Hennawi et al. 2015; Cai et al. 2017), but not all (Herenz et al. 2015).

With integral field unit spectrometers (IFUs) such as MUSE (Bacon et al. 2015), or deep imaging surveys as SILVERRUSH (Ouchi et al. 2018), the number of detailed Ly α observations – that is, spectra and sometimes surface-brightness information – exceed thousands. There are far fewer observations of polarized Ly α (Prescott et al. 2011; Hayes et al. 2011; Humphrey et al. 2013; Beck et al. 2016; You et al. 2017). This is partially due to the observational difficulty associated with polarization measurements of distant sources. Polarization-equipped instruments have presently small fields of view (FOV), and multiplexed observations of the Stokes parameters is generally hard. However, another reason is a lack of theoretical foundation which makes Ly α polarization results difficult to interpret. This is something we wish to improve upon with this work.

Presently, there are two ways of implementing polarized Ly α transfer in numerical codes. The *first* approach treats polarization solely in the macroscopical sense, and assumes that all photons are 100% linearly polarized, by ‘carrying’ a polarization vector in addition to its direction vector and frequency (Angel 1969; Rybicki & Loeb 1999; Dijkstra & Loeb 2008; Trebitsch et al. 2016). The *second* approach is that of Lee et al. (1994) (also used in Lee & Blandford 1997; Lee & Lee 1997; Lee & Ahn 1998; Lee 1999; Ahn & Lee 2015; Chang et al. 2017), who employ a quantum mechanically precise treatment of scattering and polarization using density matrices, allowing unpolarized photons to *develop* polarization through scatterings (and also allowing polarized photons to become *depolarized*). We employ this latter method, as it

is quantum mechanically more accurate, and implement it in the Monte-Carlo radiative transfer code `tlac` (Gronke & Dijkstra 2014).

The goal of this paper is to explore what additional information is encoded within the polarization properties of $\text{Ly}\alpha$ on the physical properties of the scattering medium. More concretely, our goal is to make go beyond the ‘standard’ predictions for intensity I , and focus on two linear polarization parameters Q and U , and to see whether this extra information can break degeneracies between different models, and this to gain a deeper physical understanding of sources of $\text{Ly}\alpha$.

This work is structured as follows: we describe the detailed numerical implementation of the density matrix formalism of $\text{Ly}\alpha$ polarization in § 2. This section is technical and can be skipped for readers who are mostly interested in the results, which we present in § 3. We discuss our results in more detail and in a broader context in § 4, before concluding in § 5.

2. LYMAN- α MONTE-CARLO POLARIZATION

Radiative transfer is the art of describing the complex and arduous journey light takes on after being emitted. The equation of radiative transfer³ illustrates this: a change in intensity at one frequency ν along an differential path length is affected by three factors: (1) attenuation, (2) emission and (3) redistribution in both space and frequency. The third factor is of paramount importance for $\text{Ly}\alpha$. It expresses any contributions into the intensity that did not originate at the same frequency or from the same direction. It is thus an integral over all frequencies and all solid angles embedded in a differential equation.

Monte-Carlo methods are the preferred way of treating radiative processes where the photons do not alter the state of the medium they travel through, but still are sensitive to the redistributions caused by scattering through it (see eg. Avery & House 1968; Lee & Lee 1997; Loeb & Rybicki 1999; Ahn et al. 2000; Zheng & Miralda-Escudé 2002; Dijkstra & Loeb 2008; Pierleoni et al. 2009; Laursen 2010) because – albeit slow – they guarantee convergence even in complex density or velocity fields.

Here, we describe the basics of polarization in § 2.1-§ 2.3, and how we implement the density matrix formalism into the radiative transfer code `tlac` (Gronke & Dijkstra 2014) in § 2.4.

2.1. Emission

$\text{Ly}\alpha$ photons are emitted at, or near, the $\text{Ly}\alpha$ resonance frequency of $\nu_0 = 2.47 \times 10^{15}$ Hz for hydrogen. We parametrize their offset from the line center through $x \equiv (\nu - \nu_0)/\Delta\nu_D$

³ For instance, given by Eq. (1) in the review by Dijkstra (2014) in its differential form.

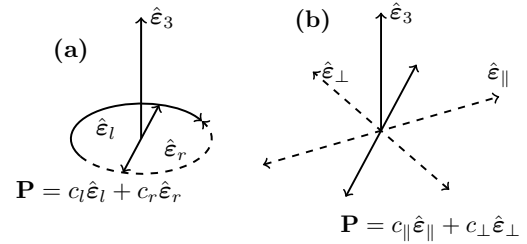


Figure 1. Conceptual sketches of two possible choices of bases in the plane perpendicular to the photon propagation direction which is chosen to be \hat{e}_3 : (a) complex, helical coordinates representative of the intrinsic spin of the photon, and (b) cartesian coordinates, representative of linear polarization appearing from a photon being in both spin states having a fixed, non-varying phase between the helical spins. The oscillations of the complex polarization vector \mathbf{P} in the plane are also drawn.

where the Doppler width is defined as $\Delta\nu_D = v_{\text{th}}\nu_0/c$ with the thermal velocity $v_{\text{th}} = \sqrt{2k_B T_g/m_p}$, which depends on the gas temperature T_g as well as Boltzmann’s constant k_B and the proton mass m_p . The speed of light is c . We also parametrize the offset from the line center in terms of the thermal velocity. The relationship is $\nu = -\lambda_0 \Delta\nu_D x$. We also represent the spread in emission around the line center as the standard deviation of a Gaussian with σ_i in units km s^{-1} .

The photons are massless and have four degrees of freedom through their two spins. Measuring the spin is synonymous to measuring their polarization. Intrinsically, the photons possess helical spins, whereas observationally, it is advantageous to consider the linear representation instead, and include a possible phase relation.

Following the approach of Lee et al. (1994), we construct a complex state vector \mathbf{P} with four degrees of freedom, represented through the complex coefficients c_1 and c_2 , given in an orthogonal basis $\{\hat{e}_1, \hat{e}_2, \hat{e}_3\}$ (where \hat{e}_3 denotes the propagation direction) as

$$\mathbf{P} = c_1 \hat{e}_1 + c_2 \hat{e}_2. \quad (1)$$

For a given \mathbf{P} , the values of the coefficients c_1 and c_2 depend on the choice of basis, which is determined by what we desire to observe: circular or linear polarization. For example, a helical basis is best suited to describe *circular polarization*, and we may use $c_1 \hat{e}_1 = c_l \hat{e}_l$ and $c_2 \hat{e}_2 = c_r \hat{e}_r$ to represent the left- and right-handed components of the spin, with probabilities $|c_l^2|$, $|c_r^2|$ of finding the photon being either left- or right-handed polarized, respectively. On the other hand, *linear polarization* arises from the superposition of the helical spins, describing it in terms of a parallel and perpendicular component, these can be written as $c_\parallel \hat{e}_\parallel = (c_l \hat{e}_l + c_r \hat{e}_r)/\sqrt{2}$ and $c_\perp \hat{e}_\perp = i(c_l \hat{e}_r - c_r \hat{e}_l)/\sqrt{2}$, respectively (see Figure 1 for a conceptual sketch of these representations of the polarization).

We may ask: if the square of the coefficients are equally large: is a polarization signal observable? The answer lies in the phase delay between the components: if both coefficients have equal magnitude *and* no fixed phase delay exists, there is no polarization. If there is a phase delay however, we will obtain a polarization signal. These additional constraints may be obtained from the cross-terms $c_1 c_2^*$ and $c_1^* c_2$. This discussion illustrates that the *density matrix* of the photon, ρ_{phot} , contains all information on its quantum state,

$$\rho_{\text{phot}} = \mathbf{P}\mathbf{P}^\dagger = \begin{pmatrix} c_1 c_1^* & c_1 c_2^* \\ c_2 c_1^* & c_2 c_2^* \end{pmatrix}, \quad (2)$$

where the off-diagonal elements give the time-dependent phase between the two states, and the diagonal elements give the probabilities of measuring the photon in either of the two states.

2.2. Scattering

After emission, the photons may scatter with neutral hydrogen gas particles⁴. This interaction excites the particle from its ground state to an intermediate state, which it immediately de-excites into its final state. Should the initial and final states be the same, the photon will neither gain nor lose any energy⁵. However, for our usage cases these effects can be ignored (Adams 1971). and the scattering is *elastic*. We will not treat inelastic Raman scattering, but refer the interested reader to Lee & Lee (1997) for an in-depth study of the polarization properties of Raman-scattered light.

When a Ly α photon elastically scatters it experiences three types of redistributions: (i) *change in propagation direction*, (ii) *change of frequency*, and (iii) the change of polarization. We discuss each below.

- **Change of propagation direction.** The change of direction is quantified by the *phase-function*, which we denote with $p(\theta', \phi' | \rho_{\text{phot}}, \theta, \phi)$. Primed quantities denote scattered values. As we describe below, this phase-function depends on frequency and polarization of a Ly α photon. It gives the probability of a photon being in the state it would obtain following a scattering, and can be directly related to the density matrix;

$$p(\theta', \phi' | \rho_{\text{phot}}, \theta, \phi) = \frac{|c_1^{2'}| + |c_2^{2'}|}{\int (|c_1^{2'}| + |c_2^{2'}|) d\Omega}. \quad (3)$$

⁴ In this work we focus exclusively on scattering by HI-atoms. Scattering by dust and electrons can be included in future studies. However, although dust clearly plays an important role in the Ly α radiative transfer process, its effect is mostly to destroy Ly α photons.

⁵ This is not entirely true. The photons deposit and gain energy through atomic recoil (Madau et al. 1997) and hyperfine excitation of the ground state (Wouthuysen 1952; Field 1958)

Each scattered density matrix component is obtained by a linear combination of the three incoming components, with trigonometric functions weighing each contribution. Expressions for the density matrix are complex (see e.g. Lee et al. 1994 or Lee 1994 for prescriptions for obtaining them, or Ahn & Lee 2015 for the relevant expressions for Ly α), and we refer interested reader to these papers. Full expressions for $c_1^{2'}$ and $c_2^{2'}$ as a function of $(\theta', \phi', \rho_{\text{phot}}, \theta, \phi)$ are given in Appendix A.

- **Change of frequency.** The ‘type’ of elastic scattering depends on the offset from the resonance frequency ν_0 , as seen from the scattering atom. We express the velocity v_{atom} of the scattering atom as a dimensionless velocity $\mathbf{u} = \mathbf{v}_{\text{atom}}/v_{\text{th}}$. The frequency shift of the Ly α photon in the rest frame of the atom, x_e , is then

$$x_e = x_i - \mathbf{u} \cdot \hat{\mathbf{k}} \quad (4)$$

where x_i was the initial frequency shift (Laursen 2010). We can differentiate between *resonance scattering* ($x_e \sim 0$) and *wing scattering* ($|x_e| \gg 0$). This distinction is important: Stenflo (1980) showed that, for resonant scattering the polarization properties of scattered Ly α relate to the *spin* properties of the atomic configuration of the H-atom. On the other hand, for wing scattering, the electron behaves as if it is free.

The transition from core to wing occurs at a temperature-dependent frequency offset $x_{c_w} \sim 3$ (see e.g. Laursen 2010, for an expression for x_{c_w}). We also use an acceleration scheme for Ly α Monte-Carlo radiative transfer as in Dijkstra et al. (2006), but have explicitly verified that our results are not affected by this.

- **Change of polarization.** The change of polarization properties is quantified by the change of the density matrix per scattering event. The newly obtained total⁶ degree of polarization of a photon P_{phot} following a scattering is the fraction of the linearly (Q and U) and circularly (V) polarized intensity to the total intensity (I),

$$P_{\text{phot}}(\theta', \phi' | \rho_{\text{phot}}, \theta, \phi) = \frac{\sqrt{Q^2 + U^2 + V^2}}{I} \quad (5)$$

$$= \frac{\sqrt{(|c_1^{2'}|^2 - |c_2^{2'}|^2)^2 + 2^2(c_1 c_2^*)'(c_1^* c_2)'}}{|c_1^{2'}|^2 + |c_2^{2'}|^2} \quad (6)$$

following Ahn & Lee (2015).

⁶ In the absence of circular polarization, $c_1 c_2^* = c_1^* c_2$ if we have chosen a linear basis. This cross term then only gives the U polarization. Otherwise it also gives the V polarization.

We now turn to discuss resonant and wing scattering in more detail, as the distinction between the two plays an important role in the above processes.

2.2.1. Resonance scattering

For $|x_e| < x_{\text{cw}}$, we will consider scatterings dominated by the transition from the ground energy state of hydrogen, denoted⁷ $1S_{1/2}$ to the excited $n = 2$ state, comprising the two available orbital configurations $2S_{1/2}$ or $2P_J$, where the $2P_J$ level is degenerate into $J = 1/2$ and $J = 3/2$, and back to the final $1S_{1/2}$ state.

This degenerate upper state with the similar angular configuration is also found in other atoms, but with larger frequency separations than $\Delta\nu = 1.1 \times 10^{10}$ Hz (Brasken & Kyrola 1998) obtained for hydrogen. We will therefore adopt the terminology from those transitions: for Ca II, the transition from $J = 1/2 \rightarrow J = 3/2 \rightarrow J = 1/2$ is denoted K (or D_2 for Na I), while for the transition $J = 1/2 \rightarrow J = 1/2 \rightarrow J = 1/2$, it is denoted H (or D_1 for Na I).

H scattering: The wave function of the $2P_{1/2}$ state has no angular dependence, and when it de-excites, conservation of momentum may result in a photon traveling in any direction, with any perpendicular polarization vector. Transitions through this state will yield a constant, angle-independent phase function, and zero polarization independent on any prior polarization,

$$p_{\text{H}}(\theta', \phi' | \rho_{\text{phot}}, \theta, \phi) = \text{const}, \quad (7)$$

with the subsequent density matrix being $|c_1^{\prime 2}| = |c_2^{\prime 2}| = 1/2$, and $c_1^{\prime} c_2^{\prime *} = c_2^{\prime} c_1^{\prime *} = 0$.

K scattering: The wave function of the $2P_{3/2}$ state, on the other hand has a strong angular dependence. The phase function now depends on all the density matrix coefficients, and hence also on the incoming polarization. We present how the density matrix elements transform in Eqs. (A5–A7), as given in Eq. (11) in Ahn & Lee (2015)⁸. These transformations are given for a left-handed photon basis, with one vector parallel to the plane of the scattering, and the other perpendicular to it. The elements of the scattered density matrix obtained here are linear combinations of the elements of the incoming matrix, where the weights are determined by the incoming and scattered angles, as well as their differences.

Core scattering: We will from now refer to the resonant H- and K-transitions collectively as *core scatterings*. The small frequency separation between the two make it difficult to determine exactly the transition type. However, we use that the effective ratio between the cross sections are $2\lambda_{\text{H}}/\lambda_{\text{K}} \approx 2$

(Stenflo 1980). In the resonance core, H-scattering is then twice as likely as K-scattering.

2.2.2. Wing Scattering

As shown by Stenflo (1980), scattering far from the line center will, due to the interference between the two available sublevels of the excited $\text{Ly}\alpha$ state, resemble that of a classic oscillator. Wing scattering may be approached as a $J = 0 \rightarrow J = 1 \rightarrow J = 0$ transition, which is the one representing Rayleigh and Thomson scattering alike (Chandrasekhar 1960). For this transition, we obtain the phase function and degree of polarization from density matrix of Eq. (4) in Ahn et al. (2002). Scattering at right angles yields 100% polarization, while light that is forward or backward scattered, retains its initial degree of polarization and the phase relation—thus preserving the polarization direction as well.

2.3. Escape and Detection

Detection is the last step involved in the Monte Carlo procedure. Observationally, polarization properties of radiation are quantified by the Stokes parameters. To construct these parameters, we need extract these from the polarization properties of individual photons in our Monte-Carlo simulation (which are quantified by the density matrix/polarization state vector \mathbf{P}).

We achieve this by constructing a 3×3 ‘observable’ density matrix ρ_{obs} which projects the complex polarization state vector \mathbf{P} (i.e. the density matrix, see Eq 2) onto the plane of the sky defined by the observer. First, we specify the direction along which we ‘observe’ our model. Without loss of generality, we define this direction to correspond to the $+z$ direction, and thus assume that plane of the sky corresponds to the xy -plane. We then only select those photons that escape within a solid angle ω from the $+z$ direction, and calculate the Stokes parameters for each photon in this subset as follows:

$$I = |c_x^2| + |c_y^2| \quad (8)$$

$$Q = |c_x^2| - |c_y^2| \quad (9)$$

$$U = c_x c_y^* + c_x^* c_y = 2c_x c_y^* = 2c_x^* c_y \quad (10)$$

$$V = i \left(c_x c_y^* - c_x^* c_y \right) = 0 \quad (11)$$

where the coefficients $|c_x^2|$, $|c_y^2|$, $|c_z^2|$ and their phase relations $c_x c_y^*$, $c_x c_z^*$ and $c_y c_z^*$ and how these relates to the (intrinsic) density matrix of the photon, ρ_{phot} are given in Appendix B. The last equalities of Eqs. (10) and (11) further indicate that we have no circular polarization as we neither have emission of circularly polarized $\text{Ly}\alpha$ or processes that induce it.

We may then proceed to create images of the binned Stokes components, either for all frequencies, or further bin the photons given their frequency. We may then define the *degree of*

⁷ We use the notation nL_J , n : energy level, $L = 0, 1, 2, 3, \dots$ denoted S, P, D, F, ... for the orbital angular momentum quantum number and $J = L + S$ where $S = \pm 1/2$ is the electron spin.

⁸ Or Eq. (5) in Ahn et al. (2002).

polarization,

$$P = \frac{\sqrt{Q^2 + U^2}}{I}, \quad (12)$$

and the relevant polarization angle,

$$\chi = \frac{1}{2} \arctan\left(\frac{U}{Q}\right), \quad (13)$$

in line with observational work (Hayes et al. 2011). The degree of polarization and the polarization angle are thus derived quantities from the primarily binned Stokes parameters we calculated for each photon. Note also that $I^2 \geq Q^2 + U^2$ (see eg. Rybicki & Lightman 1979), meaning that both Q and U may be zero when the intensity is not.

We have tested our implementation against known solutions. In Appendix C.1 we have tested our code against scattering of a plane parallel, semi-infinite slab known from Chandrasekhar (1960) for which Ahn & Lee (2015) also obtained results; against scattering in a Hubble-expanding cosmological volume known from Rybicki & Loeb (1999) in Appendix C.2; and against the expanding shell of Dijkstra & Loeb (2008) in Appendix C.3. The density matrix implementation in `tlac` yields equal results to those of Ahn & Lee (2015). Additionally, it reproduces the degree of polarization as well as the surface brightness profiles for the expanding IGM and outflowing shell, even though the results that were compared to were obtained with the approach of Angel (1969), ie. with fully polarized photons.

2.4. Monte Carlo Implementation Summary

We implement the density matrix formalism for polarization into `tlac` as follows:

1. We assign a 2×2 (possibly complex) density matrix ρ_{phot} to each photon. We emit photons in a random direction (θ, ϕ) , and unpolarized. In practise this means that we assign a density matrix with $|c_1^2| = |c_2^2| = 1/2$ with no time-dependent correlation between them, i.e. $c_1 c_2^* = c_2 c_1^* = 0$.
2. We generate an HI optical depth τ from the distribution $\exp(-\tau)$, and convert τ into a physical distance s the Ly α photon travels before it escapes, by solving the line integral $\tau = \int_0^s dr' n_{\text{HI}}(r') \sigma_{\alpha}(v[r'])$ (see Gronke & Dijkstra 2014 for a more extended description of the code).
3. The new propagation direction after scattering depends on the phase-function, which depends on the density matrix, which depends in turn on the type of scattering event (H vs K vs wing), and the density matrix of the photon prior to scattering.

The frequency of the photon determines whether the scattering occurs in the damping wing or in the core.

For wing scattering the post-scattering density matrix is given by⁹ Eqs. (A8–A10). For core scattering, we draw a random number $\mathcal{R} \sim \text{Unif}[0, 1)$. If $\mathcal{R} > 1/3$ the scattering is H-type and the photon is depolarized ($\rho'_{\text{phot},00} = \rho'_{\text{phot},11} = 1/2$, other elements zero). Otherwise, the scattering is K-type and the post-scattering density matrix is given by¹⁰ Eqs. (A5–A7). We sample from these density matrices using the rejection method: we draw a random set of trial polar angles θ', ϕ' uniformly from a sphere, and calculate the corresponding post-density density matrix ρ'_{phot} ,

$$\rho'_{\text{phot}} = f(\theta', \phi' | \rho_{\text{phot}}, \theta, \phi), \quad (14)$$

which in turn translates to the phase function, Eq. (3). The phase function returns a number, which we compare to a randomly drawn number $\mathcal{R} \sim \text{Unif}[0, 1)$. If $p(\theta', \phi' | \rho_{\text{phot}}, \theta, \phi) \geq \mathcal{R}$, we accept the proposed scattering angles θ', ϕ' as well as the scattered density matrix ρ'_{phot} and the photon moves on.

4. To create observable, well-defined Stoke parameters, the density matrix ρ_{phot} can be transformed into a 3×3 density matrix ρ_{obs} using Eqs. (B15–B23) that is relative to the observer, which is equivalent to observing the photons with a photon counting device that is fixed in space and no longer is oriented perpendicular to the propagation direction of the photon. This introduces six new density matrix coefficients $|c_x^2|, |c_y^2|, |c_z^2|, c_x c_y^* = c_x^* c_y, c_x c_z^* = c_x^* c_z, c_y c_z^* = c_y^* c_z$.
5. For a chosen coordinate axis (which one observes nadir), there will be a plane spanned by the other two coordinate vectors. For this plane, we obtain well-defined Stokes parameters I, Q, U and V (the latter is zero) through Eqs. (8–11).
6. The Stokes parameters of each photon can be binned (by eg. frequency, radial bins, spatial pixels) to create observables for the chosen plane. Multiple planes can be combined by assuming symmetries to increase the signal-to-noise ratio. We choose to observe photons escaping within a cone of $\cos 18^\circ = 0.95$ of the axis observed nadir, similar to Trebitsch et al. (2016), who chose 15° and did not find the choice to strongly affect the results.

3. RESULTS

Ly α radiative transfer through the interstellar and circumgalactic environments is a complex problem, and it is yet unclear which physical processes and scales play an important

⁹ See also Eq. (4) in Ahn et al. (2002).

¹⁰ See also Eq. (11) in Ahn & Lee (2015).

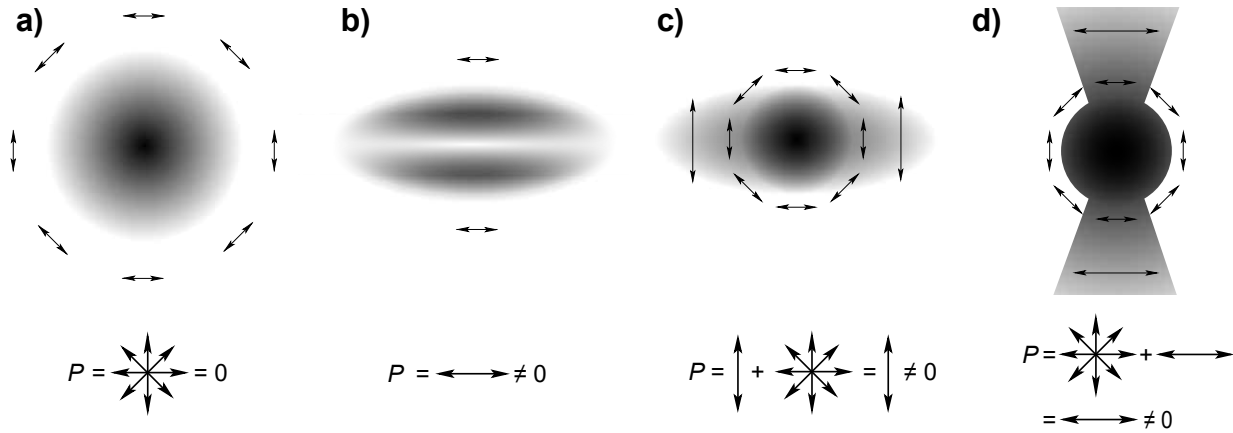


Figure 2. Sketches of four possible scattering geometries and their polarization signatures: **(a)** spherically symmetric scattering geometry where the polarization increases toward the limb and is tangential to it, **(b)** an oblate ellipsoid where the majority of the intensity is polarized parallel to the plane of the major axes, **(c)** an optically thinner ellipsoidal scattering geometry where the majority of the intensity is polarized perpendicular to the major axes and **(d)** a bipolar outflow where the polarization always is perpendicular to the outflow axis and a symmetrically polarized unobscured central core. *In the lower panels, we give the polarization if these extended sources were viewed edge-on as point sources, yielding (a) zero polarization as all vectors cancel due to the circular symmetry of the extended polarization signal, where photons that escape further out do so by scattering increasingly closer to 90° , leaving in sum a polarization signal that increases radially and that always is oriented tangentially to the central source; (b) non-zero polarization for an ellipsoid as the photons scatter and escape through optically thinner funnels along the minor axis of the ellipsoid before scattering at right angles toward the observer, becoming polarized horizontally; (c) non-zero polarization oriented perpendicular to the major axes of the ellipsoid as the scattering geometry was thin enough to allow photons to scatter along the major axes and then toward the observer, with the only allowed polarization being in the vertical direction; and (d) non-zero polarization oriented perpendicular to the outflow axis, as all the contributions from the brighter core are canceled out. The shade indicates the intensity.*

role in it. It is therefore advantageous to study $\text{Ly}\alpha$ radiative transfer in simplified geometries in order to better identify the precise origins of the predicted observables, that is, in our case the predicted polarization signal. Here, we present calculations of $\text{Ly}\alpha$ polarization for a suite of simplified systems that have been adopted in the literature. These are representative of features in more complex astrophysical systems. In particular, we will discuss:

- static (§ 3.1) or expanding (§ 3.2) ellipsoids,
- biconical outflows (§ 3.3), and
- clumps of HI clouds, representative of a multiphase medium (§ 3.4).

This can be thought of as a sequence in asymmetry: *first:* we introduce asymmetry in the gas distribution, *second:* we add an asymmetry in velocity space, *third:* we introduce further geometrical complexities by introducing biconical outflows, *fourth:* finally, we introduce ‘multiphase’ versions of the outflow models. For each model, we will introduce the model parameters and present computed $\text{Ly}\alpha$ observables that could shed light on the nature and geometry of the sources and their environment. We sketch these models and some of our findings in Figure 2, which will be referred to throughout the text. Note that the apparent geometry of a system can change with frequency as $\text{Ly}\alpha$ photons of different frequencies escape at different spatial locations.

Following Lee & Ahn (1998), we focus on computing the *frequency-dependence* of polarization for point sources, which differs from more recent analyses, which focused on (frequency-)integrated properties of spatially extended sources (Dijkstra & Loeb 2008; Dijkstra & Kramer 2012; Trebitsch et al. 2016). This may represent a case where the $\text{Ly}\alpha$ source is spatially unresolved, or a case in which a spectroscopic slit is wide enough to cover the entire source. For these point sources, we also show the total (i.e. integrated over frequency) polarization signal and its direction (relative to the unobservable geometry of the source in the plane of an observer).

3.1. Oblate Ellipsoids

Angel (1969) showed that Thomson scattering of thermal X-rays emanating from an ellipsoidal scattering geometry could provide up to 5% polarization, if it was viewed from the side as a point source. This was further explored by Kim et al. (2007), who considered $\text{H}\alpha$ line and continuum radiation emanating from an ellipsoid which also acted as a Rayleigh scatterer. They found a viewing angle-dependent increase in polarization in the wings.

We pursue this idea further for $\text{Ly}\alpha$. We run a set of simulations where we explore the effects of **(i)** changing the column density of neutral HI gas, and **(ii)** changing the ellipticity. Changing the column density is known to have profound effect on the emergent spectrum. However, as shown in Dijk-

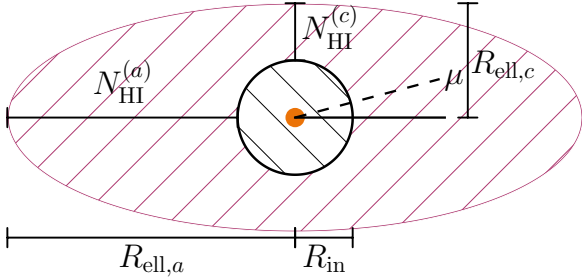


Figure 3. Ellipsoidal scattering geometry. We have an ionized, inner region of radius R_{in} where our Ly α source is located, and an outer, ellipsoidal HI region with principal axes ($R_{\text{ell},a}$, $R_{\text{ell},b}$, $R_{\text{ell},c}$) where $R_{\text{ell},a} = R_{\text{ell},b}$. The outer ellipsoid has neutral hydrogen column densities $N_{\text{HI}}^{(a)}$ and $N_{\text{HI}}^{(c)}$ along the principal axes. The viewing angle is given as μ .

stra et al. (2016), the shape of the spectrum emanating from a source region fully enclosed in an ellipsoid will primarily be given by the axis of lowest column density, and therefore it cannot reveal the ellipticity.

We create an ellipsoid of static HI gas with fixed number density n_{HI} with principal axes ($R_{\text{ell},a}$, $R_{\text{ell},b}$, $R_{\text{ell},c}$) where we set the major axes $R_{\text{ell},a} = R_{\text{ell},b}$ and the perpendicular minor axis $R_{\text{ell},c}$. This ellipsoid embeds an inner, ionized region with radius R_{in} . In this inner region, we find our source of unpolarized Ly α . The column densities along the principal axes can be found as $N_{\text{HI}} = n_{\text{HI}}(R_{\text{ell}} - R_{\text{in}})$, i.e., the neutral hydrogen number density is constant throughout the system. The viewing angle μ is defined relative to the plane of the two major axes (see Figure 3 for a sketch of this geometry).

We choose three initial column densities along the minor axis, $N_{\text{HI}}^{(c)} = 10^{17}, 10^{19}, 10^{21} \text{ cm}^{-2}$. The choice of column densities reflect those expected in real systems (Verhamme et al. 2017; Hashimoto et al. 2017; Gronke et al. 2015) The lower bound, $N_{\text{HI}}^{(c)} = 10^{17} \text{ cm}^{-2}$, corresponds to a case from which ionizing LyC may escape. The upper bound $N_{\text{HI}}^{(c)} = 10^{21} \text{ cm}^{-2}$ corresponds roughly to the upper envelope of N_{HI} that is inferred from Ly α emitting galaxies. We then vary the ellipticity by varying the major axes (i.e. $R_{\text{ell},a}$ and $R_{\text{ell},b}$). This gives a set of ellipticities

$\varepsilon \equiv R_{\text{ell},c}/R_{\text{ell},a} = \{1, 1/2, 1/10, 1/100\}^{11}$. We fix $R_{\text{in}} = 10$ pc and $R_{\text{ell},c} = 20$ pc and note that the choice of scale is arbitrary¹² for media that are static or have constant velocity fields. Our results are thus not scale-dependent. Furthermore, we set the gas temperature to $T = 10^4$ K and inject the photons with $\sigma_i = 200 \text{ km s}^{-1}$.

In Figure 4a, we plot the spectra of the intensity I and the polarization P for the emergent photons for $N_{\text{HI}}^{(c)} = 10^{21} \text{ cm}^{-2}$ and all ellipticities, viewed with $\mu = 0$ (edge-on). As a guide to the eye, we plot (in this and other intensity spectra) a gray dashed line, centered at 160 km s^{-1} . This velocity offset marks a typical boundary between the redward, observable part of the spectrum, and the blueward, inaccessible part, for which the increasingly neutral IGM at higher z prevents transmission of Ly α photons (Dijkstra et al. 2007; Laursen et al. 2011).

As we are effectively changing the column density of the major axis, and the (I) spectra do not change, we realize that their shape are given by the column densities along the minor axis, which does not change, and not along the line of sight (LOS). In other words, the spectrum is mostly determined by the HI column density along the path of ‘least resistance’ (see also Dijkstra et al. 2016 for a similar result). However, we find that P is overall higher across the spectrum for increased ellipticities, including at those frequencies where most photons escape. This can be understood as a consequence of the increasing deformation of the source with increasing ellipticity. At all frequencies, the shape of the source becomes asymmetric, leaving a preferential polarization direction and an overall non-zero polarization signal.

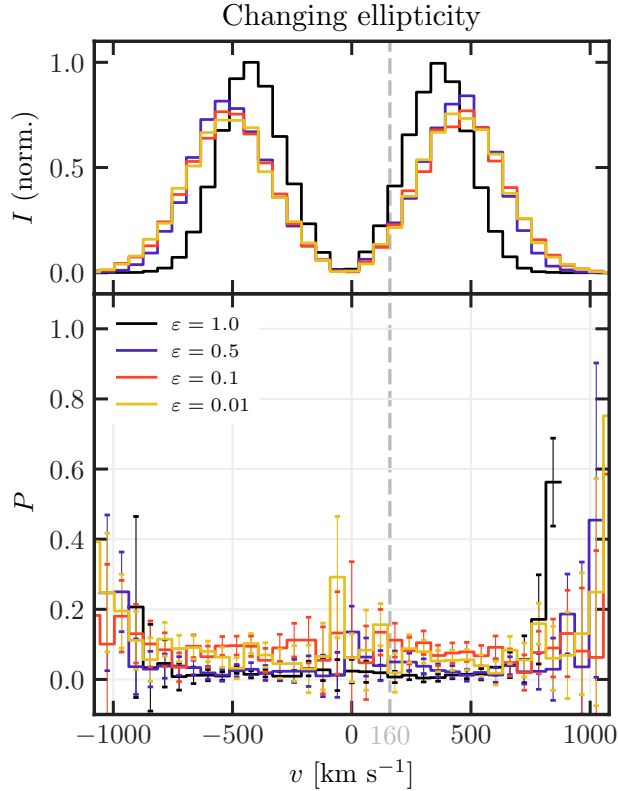
We quantify this effect in Figure 4b. Here we show the fractional degree of polarization P as a function of (i) the minor axis column density $N_{\text{HI}}^{(c)}$ and (ii) the ellipticity ε . We assumed that we view the sources edge-on¹³ (i.e. the projected size of the source is $R_{\text{ell},c} \times R_{\text{ell},a}$). The color of a bin indicates the degree of polarization. The arrow indicates the direction of the linear polarization w.r.t the plane of the major axes (the size of the arrow also reflects its magnitude).

The lower 3 panels of Figure 4b show that the degree of polarization is $P < 1\%$ for a spherical scattering geometry ($\varepsilon = 1$), as the spherical symmetry washes out any polarization. The polarization increases with ellipticity, but in a way that depends non-trivially on $N_{\text{HI}}^{(c)}$: the direction of the polarization vector changes as $N_{\text{HI}}^{(c)}$ increases from $N_{\text{HI}}^{(c)} = 10^{19} \text{ cm}^{-2}$ to $N_{\text{HI}}^{(c)} = 10^{21} \text{ cm}^{-2}$. This change in column density

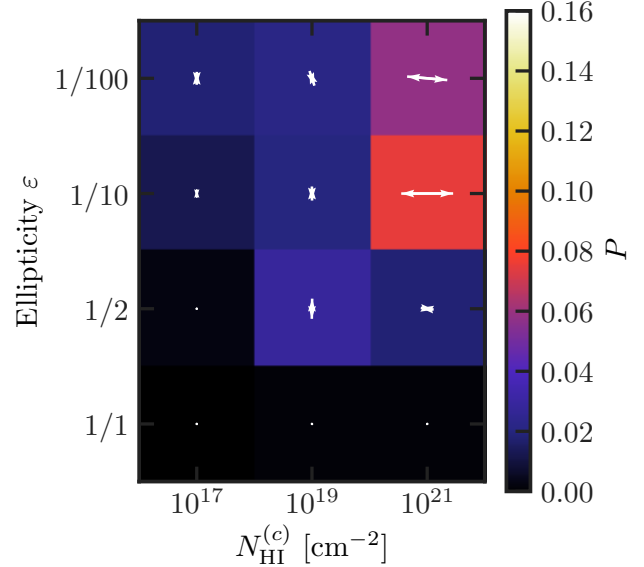
¹¹ A change in ellipticity is equivalent with changing the column density along the major axes, $N_{\text{HI}}^{(a)}$.

¹² However, the choice of the ratio $R_{\text{in}}/R_{\text{ell},c}$ may not be, we have however not investigated this further.

¹³ Face-on sources would appear circularly symmetric, and any polarization signal averages out.



(a) Intensity (normalized to unit area under curve) and polarization spectra as function of velocity offsets from the $\text{Ly}\alpha$ line center for ellipsoids with $N_{\text{HI}}^{(c)} = 10^{21} \text{ cm}^{-2}$ along the minor axis, $T = 10^4 \text{ K}$, viewed edge-on as point sources. The colors indicate their ellipticities, given as the ratio between the minor and major axes, $\varepsilon \equiv R_{\text{ell,c}}/R_{\text{ell,a}}$. The vertical dashed, grey line indicates a typical velocity offset where photons blueward commonly are seen to be absorbed by the IGM. Hence, the spectrum blueward of the dashed line is in many cases not detectable.



(b) The degree and direction of polarization for ellipsoids with varying column densities along the minor axis, $N_{\text{HI}}^{(c)}$ and varying ellipticities ε . The ellipsoids are viewed edge-on, i.e. where they appear to be asymmetrical, but as point sources to prevent introduction of non-intrinsic geometric asymmetries by for example a narrow slit viewing only parts of the overall source. Viewed face-on, i.e. where the ellipsoids would have appeared symmetric to an observer, the total polarization is zero for all ellipticities and column densities, unlike in this plot. The direction of the arrows indicate the polarization direction relative to the plane of the major axes: horizontal arrows are parallel to it, whereas vertical arrows are perpendicular to it.

Figure 4. Static ellipsoids with varying ellipticity and column density along the minor axis, $N_{\text{HI}}^{(c)}$.

effectively blocks all light from the central part of the system, leaving only photons that escape along the minor axes. See panel b) of Figure 2 for a sketch of this obscuration. To reach the observer, they have to scatter closer to 90° , obtaining large degrees of polarization with the polarization vector oriented parallel to the major axes. This effect is fundamentally similar to the effect seen in spherically-symmetric systems. At large radii, photons also are highly polarized as they must escape these systems at 90° to reach the observer, see e.g. the rise in P with radius in Figure 3 of [Dijkstra & Loeb \(2008\)](#). The polarization direction is always tangential to the central source. In these systems, the global signal would be canceled out from symmetries, however, as illustrated in panel a) of Figure 2.

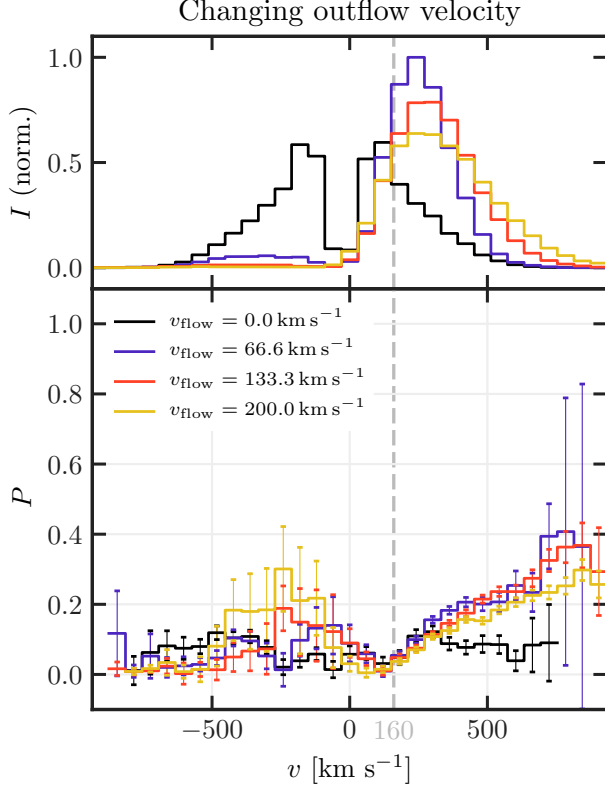
3.2. Expanding Ellipsoids

The previous section discussed the polarization emerging from static ellipsoids. Here, we add an outflowing

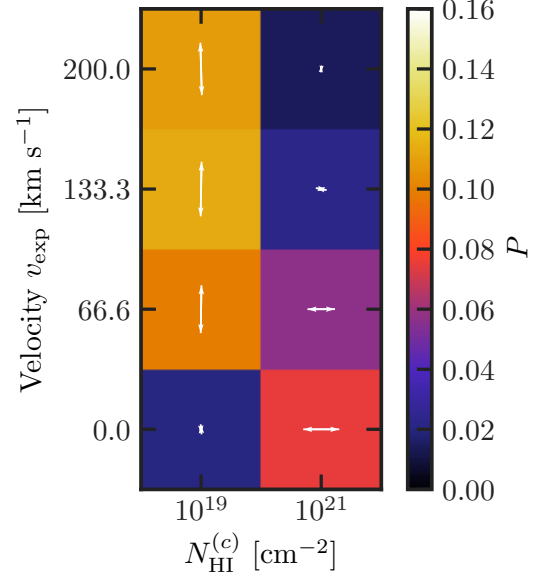
component to the ellipsoid with constant velocities $v_{\text{flow}} = \{0, 67, 200\} \text{ km s}^{-1}$, which is directed radially outward. As in § 3.1 we fix $\sigma_i = 200 \text{ km s}^{-1}$. The presence of an outflow introduces an additional degree of asymmetry, now in velocity space.

Figure 5a shows the spectrum and frequency-dependence of the polarization emerging from sources with fixed $N_{\text{HI}}^{(c)} = 10^{19} \text{ cm}^{-2}$ along the minor axis, ellipticity $\varepsilon = 1/10$, but with different expansion velocities v_{flow} . For the static case we recover the double peaked spectrum that we obtained in § 3.1. Expansion causes the majority of the photons to escape in the red wing, as blueward photons experience a higher optical depth (see e.g. [Zheng & Miralda-Escudé 2002](#); [Ahn et al. 2003](#); [Dijkstra et al. 2006](#)).

The frequency dependence of the polarization is also asymmetric around the line center. For the cases with $v_{\text{flow}} \neq 0$, there is little flux on the blue side of the line. The polarization of this flux is comparable to that of the



(a) Intensity and polarization spectra for ellipsoids with ellipticity $\varepsilon = 1/10$, column density $N_{\text{HI}}^{(c)} = 10^{19} \text{ cm}^{-2}$ along the minor axis, $T = 10^4 \text{ K}$, with varying degrees of global outflow velocities v_{flow} indicated by the line color. The expanding ellipsoids are viewed edge-on. The grey dashed line indicates the threshold for IGM removal of photons.



(b) Total degree of polarization and its direction (given by the arrows) relative to the plane of major axes for globally expanding ellipsoids with outflow velocities v_{exp} , ellipticity $\varepsilon = 1/10$, and column densities along the minor axis $N_{\text{HI}}^{(c)}$. The spectra of the sources with $N_{\text{HI}}^{(c)} = 10^{19} \text{ cm}^{-2}$ are plotted in Figure 5a.

Figure 5. Expanding ellipsoids with varying outflow velocity and column density along the minor axis, $N_{\text{HI}}^{(c)}$.

static case (within the uncertainties). On the other hand, in the red wing of the line, outflows enhance the degree of linear polarization significantly. We obtain an increasing degree of linear polarization with velocity offset Δv from the line center that approaches $P \sim 30\%$ asymptotically at $\Delta v > 500 \text{ km s}^{-1}$. It is remarkable that the increase in the degree of linear polarization is very similar for all models with $v_{\text{flow}} \neq 0$. This result can be understood as follows. The distance a photon can travel increases for increasing outflow velocities, effectively lowering the optical depth seen by the photons. In our cases, the change in outflow velocities would not necessarily imply a change in observed spatial shape of the system. The optical depth is sufficiently low to make a significant fraction of the photons diffuse along the major axes in the presence of outflows, with polarization vectors tangential to the direction of the central source, as sketched in panel c) of Figure 2. This means that the spatial asymmetry does not change significantly, and the degree of polarization remains similar between the models.

Figure 5b shows the degree and direction of polarization of expanding ellipsoids with $N_{\text{HI}}^{(c)} = \{10^{19}, 10^{21}\} \text{ cm}^{-2}$ and

$\varepsilon = 1/10$ viewed edge-on. We omit the case $N_{\text{HI}}^{(c)} = 10^{17} \text{ cm}^{-2}$, because we found that for this case, too few photons scatter, and our predictions practically correspond to that assumed for the intrinsic source. For $N_{\text{HI}}^{(c)} = 10^{19} \text{ cm}^{-2}$, the polarization is near zero for the static ellipsoid (in agreement with the *central upper panel* of Figure 4b). When we increase v_{flow} , the polarization remains roughly constant $P \sim 10\%$, with the polarization direction aligned perpendicular to the major axes. This can be understood to be of the same reasons the degree of the polarization in the spectra did not change. The spatial (observed) shape of the systems do not significantly change for the increasing outflow velocities. As the asymmetries do not change, the systems obtain similar degrees and directions of polarization.

Figure 5b contains other interesting results: For a higher column density along the minor axis, $N_{\text{HI}}^{(c)} = 10^{21} \text{ cm}^{-2}$, the polarization behaves completely different compared to the case $N_{\text{HI}}^{(c)} = 10^{19} \text{ cm}^{-2}$. The total polarization of $P = 8\%$ for a static ellipsoid (see also Figure 4b), and it now *decreases* with outflow velocity, reaching $P = 1\%$ for $v_{\text{flow}} = 200 \text{ km s}^{-1}$. For this higher column density, the system is seen tran-

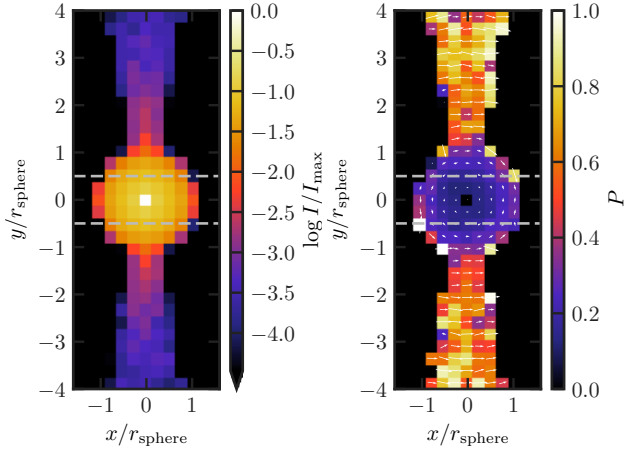


Figure 6. Spatially extended maps of the intensity and degree of polarization for bipolar outflows of $v_{\text{flow}} = 200 \text{ km s}^{-1}$ from a static sphere with $N_{\text{HI}} = 10^{19} \text{ cm}^{-2}$ and a total opening angle of $\theta_{\text{flow}} = \pi/8$. The color indicate the degree of polarization, and the arrows indicate the direction of polarization. The dashed lines indicate the region that is obscured in Figure 8, to resemble the removal of $\text{Ly}\alpha$ photons by for example a dusty disk.

sitioning from the state sketched in panel b) in Figure 2 to the more symmetric case presented in panel c). However, there is one important difference from the system presented in panel c) as well as the system with lower column density $N_{\text{HI}}^{(c)}$. The increase in optical depth from the increased column density means that the photons also increasingly scatter once they encounter the rest-frame velocity offset of the atoms in the expanding medium. This isotropizes the local radiation field, and the polarization vectors become randomized. The lowering in optical depth from the increasing outflow means the photons penetrate deeper also along the major axes, contributing to removing the spatial asymmetry. The overall effect is that the net polarization is reduced. This reduction is eventually accompanied by a flip in the polarization vector of the $N_{\text{HI}}^{(c)} = 10^{21} \text{ cm}^{-2}$ system, where the vector changes alignment from being parallel to perpendicular to the major axes. This indicates an increased semblance to the geometry of the much lower column density system $N_{\text{HI}}^{(c)} = 10^{19} \text{ cm}^{-2}$.

3.3. Bipolar Outflows

So far, our analysis has focused on spherically or cylindrically symmetric gas geometries. However, there is observational and theoretical evidence that outflows are bipolar (e.g. Blandford & Rees 1974; Suchkov et al. 1994). More recently, observations of LARS 05 (Duval et al. 2016) nicely illustrate how $\text{Ly}\alpha$ photons scatter off a bipolar outflow that burst out of an edge-on disk galaxy. In this section, we focus on predicting spectra and polarization of scattered $\text{Ly}\alpha$ radiation emerging from simplified representations of bipo-

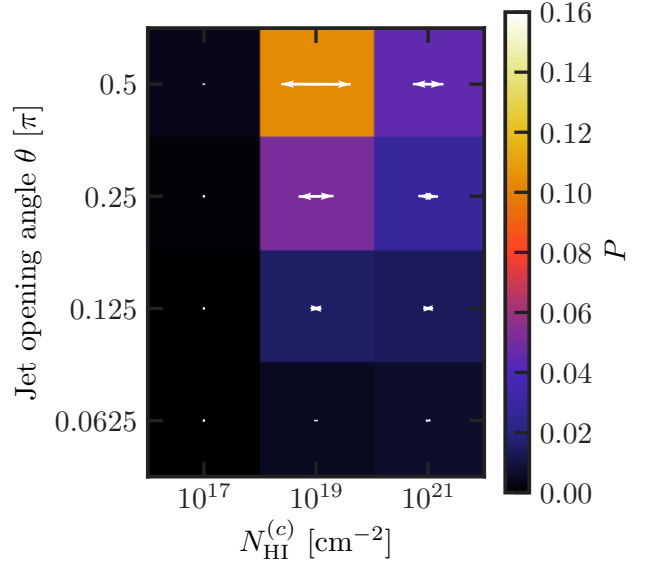


Figure 7. Degrees of polarization had the unobscured bipolar flows (with outflow velocity $v_{\text{flow}} = 200 \text{ km s}^{-1}$) been viewed as a point source. Direction of overlaid polarization vectors indicate their direction relative to the flow (horizontal: perpendicular to flow directions, vertical: parallel to flow directions).

lar outflows, with either an unobscured (§ 3.3.1) or obscured (§ 3.3.2) central source.

We model the bipolar outflows as follows: it contains a spherical cloud with either $N_{\text{HI}} = \{10^{17}, 10^{19}, 10^{21}\} \text{ cm}^{-2}$ and $T = 10^4 \text{ K}$ that resides in a fully ionized environment. The (unpolarized) $\text{Ly}\alpha$ source resides in the center of this cloud. We then introduce bipolar outflows in cones with total opening angles $\theta_{\text{flow}} = \{1/16, 1/8, 1/4, 1/2\}\pi$. Inside the cones, gas is radially outflowing with a constant velocity $v_{\text{flow}} = 200 \text{ km s}^{-1}$. The HI number density in the cones is equal to that in the central sphere, and extend a factor of 4 further than the edge of the sphere.

3.3.1. Unobscured Central Source

Figure 6 shows an illustrative example of the spatial distribution of intensity and polarization for an outflow with $\theta_{\text{flow}} = \pi/8$ viewed edge-on¹⁴. We clearly see the biconical structure in both the intensity and the polarization images. In the central, static sphere, the degree of polarization increases familiarly toward the limb, reaching $P \sim 30\%$ with the polarization angle oriented tangentially to the center. The intensity decreases radially outward, both in the central cloud and in the cones. This diffusion of photons gives rise to a de-

¹⁴ When viewing the outflows face on, i.e. straight into the cones and possibly also the central static cloud, one would observe a spherically symmetric source, and hence would any point source polarization signal be lost.

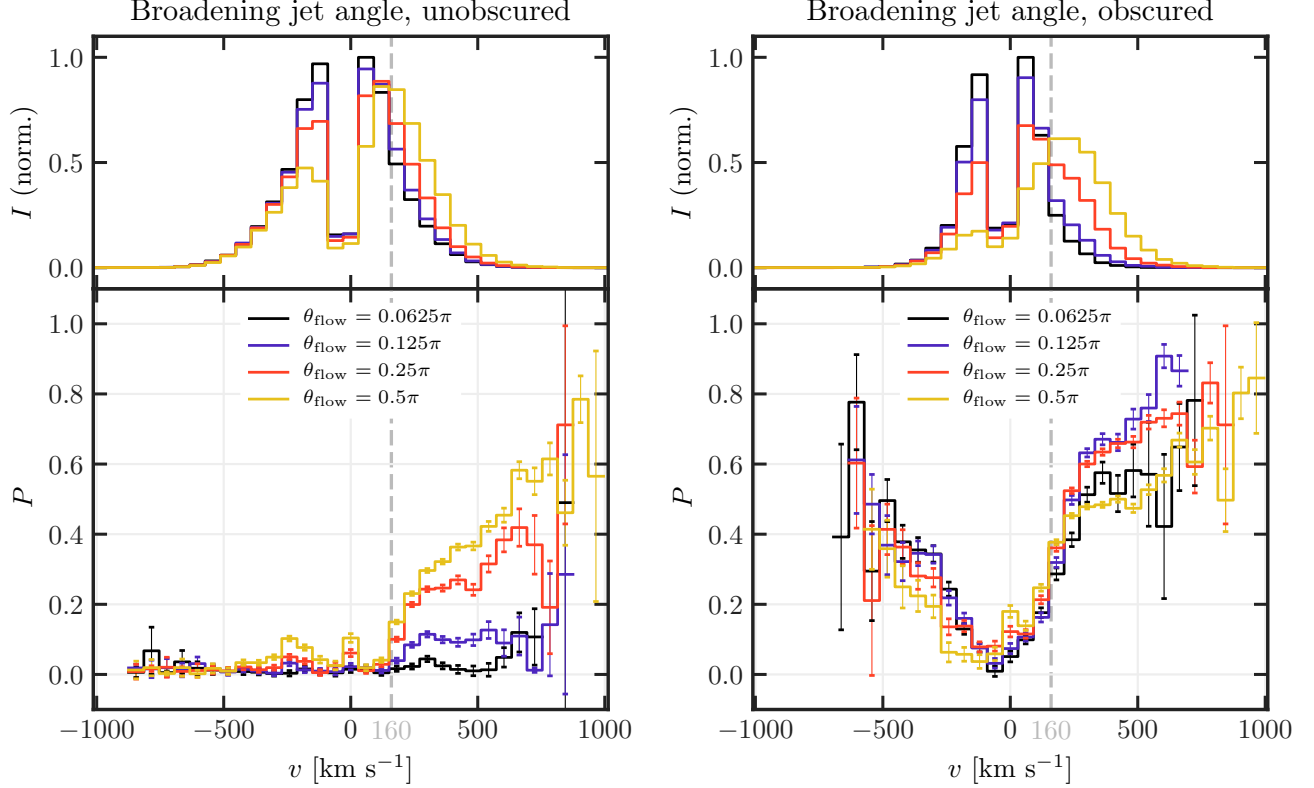


Figure 8. Intensity and polarization spectra for bipolar outflows with $v_{\text{flow}} = 200 \text{ km s}^{-1}$ out of a static HI non-elliptic sphere with radial column density $N_{\text{HI}} = 10^{19} \text{ cm}^{-2}$. The opening angle θ_{flow} of the outflows out of the sphere is indicated by the line colors. The grey, vertical dashed lines indicate the velocity offset for which bluer photons would be removed by a partially neutral IGM. **Left:** spectra for unobscured sources, i.e. including photons leaving both the central, static sphere and the moving medium in the bipolar cones. **Right:** spectra for partially obscured sources, i.e. corresponding to blocking photons emitted within the horizontally dashed grey lines in Figure 6, resembling for example the removal of Ly α photons by a circumgalactic disk of dust.

ing surface brightness profile, see e.g. Figure 4 of [Dijkstra et al. \(2006\)](#). In the outflows, the degree of polarization increases with Δv reaching values of $P \sim 50\% - 70\%$ (pixels with $P > 80\%$ exist, but the flux in these is negligible). The direction of polarization in the outflows are oriented perpendicular to the flow direction.

Figure 6 also shows that the overall degree of polarization signal increases with the opening angle θ_{flow} and is always aligned perpendicular to the outflow direction. This is the same physical effect that we saw at play for the ellipsoids: the local radiation fields are stronger in the direction of the source, and are not isotropized, leaving a polarization vector tangential to the direction of the central source.

The dependence of integrated polarization on θ_{flow} is summarized in Figure 7, which shows clearly that P increases with θ_{flow} for all $N_{\text{HI}}^{(c)}$. This increase reflects that a increasing θ_{flow} causes a larger fraction of flux to emerge from the biconical outflows, thereby increasing the spatial asymmetry of the source. Additionally, the biconical outflows appear as more polarized: fewer photons scatter here. Those that do, propagate along the outflow direction, but have to scatter and

escape at angles closer to 90° to reach the observer. That way they gain large degrees of polarization that also are oriented perpendicular to the outflow axis. We illustrate this in panel d) of Figure 2.

Figure 7 also shows that the overall polarization is maximal for $N_{\text{HI}} = 10^{19} \text{ cm}^{-2}$. For $N_{\text{HI}} = 10^{17} \text{ cm}^{-2}$, the central cloud is optically thin to most emitted Ly α photons, and there is little flux in the scattered component (and the flux that does scatter, scatters in the core which leads to a lower degree of polarization). The overall polarization for $N_{\text{HI}} = 10^{21} \text{ cm}^{-2}$ is lower because in this case, the scattering medium is optically thicker, which isotropizes the Ly α radiation field. In turn, this isotropization reduces the overall polarization of the radiation that escapes.

The *upper left panel* of Figure 8 shows the spectra of the models with $N_{\text{HI}} = 10^{19} \text{ cm}^{-2}$ (i.e. with maximum polarization). The spectra are double-peaked, with the red peak becoming stronger relative to the blue peak with increasing θ_{flow} . This increase reflects the increasing fraction of Ly α photons that scatter through the outflow. The *lower left panel* of Figure 8 shows that the degree of polarization is negli-

ble blueward of line center for all opening angles. Redward, the degree of linear polarization increases with $\Delta\nu$. This reflects that the blue peak consists of photons that escape from the static central cloud: polarization is canceled out from the symmetric central geometry (as for case *a* in Figure 2). This also holds to some extent for the red peak, but in addition, it has contributions from photons that have escaped into the biconical outflows. There, they scatter less and provide a higher overall local polarization signal. The redward increase in the global polarization reflects the increasing spatial asymmetry with $\Delta\nu$.

3.3.2. Obscured Central Source

We repeat the previous analysis (§ 3.3.1), but now obscure the central static sphere (the obscured region is indicated with *grey dashed lines* in Figure 6). This represents a case in which the biconical outflows are separated by for example a dusty galactic disk as in LARS 05 (see Duval et al. 2016) or in M82 (Lynds & Sandage 1963; Gallagher & Smith 1999).

The *right panels* of Figure 8 show the spectra & polarization for the same models as in the *left panels*, but with the central region obscured. Especially the red peaks of the spectra are widened for the largest opening angles $\theta_{\text{flow}} = \{1/4, 1/2\}\pi$. This enhancement of the red peak is primarily a renormalization of the entire spectrum. The obscuration removes a majority of the (blue and red) photons that arise from the central spherical cloud, leaving the surplus of red photons that escape from the cones. For smaller opening angles θ_{flow} however, less of the overall flux originates from the bipolar cones. The surplus of red photons that was seen for the larger opening angles is present, but is however not sufficient to significantly alter the shape of the spectrum. The spectral signature of the outskirts of the central sphere therefore dominate the spectrum.

The *lower right panel* shows that the polarization increases at effectively all frequencies. This simply reflects that obscuring the central source eliminates photons whose polarization vectors align with the cone axis. The polarization in the blue wing is lower than in the red wing, as these are photons that escape from primarily the central sphere. The additional boost in P at large $\Delta\nu$ in the red wing is the signature of the photons that have scattered in the outflows. As for the unobscured case, the local polarization is higher due to the fewer scatterings photons here undergo, and the global degree of polarization reflect the spatial asymmetry due to the cones. The degree of polarization in the red wing reveals how the source transitions from nearly symmetrical without much contributions from the cones for $\theta_{\text{flow}} = 1/16$, to larger contributions from the cones with increasing θ_{flow} . This comes at a price: the increased opening angles also allow for larger variations in the polarization vectors which in the cones are tangential to the source.

3.4. Multiphase Medium

All previous models represented gas in the ISM with a single density and temperature. In reality, interstellar (and circum-galactic) gas is known to be multi-phase. $\text{Ly}\alpha$ radiative transfer through multiphase media is a complex problem, which has also been represented by simplified models (see e.g. Neufeld 1991; Hansen & Oh 2006; Dijkstra & Kramer 2012; Laursen et al. 2013; Gronke & Dijkstra 2016). These simplified models consist of neutral, spherical (possibly dusty) clumps, embedded within a hot, ionized and dust free medium (based loosely on the early models by McKee & Ostriker 1977).

It has been demonstrated that for such ‘clumpy’ media, the key parameter that affects $\text{Ly}\alpha$ radiative transfer is the average number of clumps per sightline: the covering factor f_c (see Hansen & Oh 2006; Gronke & Dijkstra 2016). Gronke & Dijkstra (2016); Gronke et al. (2017) showed that there exists a critical value for f_c , $f_{c,\text{crit}}$, above which clumpy media affect $\text{Ly}\alpha$ photons as if they consist of a single phase (i.e. homogeneous). The value of $f_{c,\text{crit}} \sim$ a few - a few tens depending on the total HI column density and kinematics of the clumps (see Gronke et al. 2017). The polarization properties of $\text{Ly}\alpha$ radiation that scatters through ‘very clumpy’ (i.e. $f_c \gg f_{c,\text{crit}}$) are therefore well captured by our previous models, in which the gas was homogeneously distributed. The polarization properties of $\text{Ly}\alpha$ radiation through models with $f_c \ll f_{c,\text{crit}}$ have been explored in Dijkstra & Kramer (2012), where it was associated with few (or no) scatterings and consequently high degrees of polarization.

In this section, we focus on the ‘transition regime’ which corresponds to $f_c \sim f_{c,\text{crit}}$, and contrast a central $\text{Ly}\alpha$ emitting source surrounded by a uniform distribution of randomly moving clumps (which can represent a central star forming galaxy surrounded by a clumpy circum-galactic medium) with a setup where the $\text{Ly}\alpha$ radiation emerges from the clumps (which can represent the same galaxy and circum galactic medium, but in which $\text{Ly}\alpha$ arises as fluorescent emission powered by ionizing radiation that leaked from the central galaxy, see Mas-Ribas & Dijkstra 2016; Mas-Ribas et al. 2017). While the numerical value of $f_{c,\text{crit}}$ depends on the neutral hydrogen column density of the clumps $N_{\text{HI,cl}}$ and their kinematics (Gronke et al. 2017), we stress that the characteristics described in this section apply generally for systems with $f_c \sim f_{c,\text{crit}}$.

In our models, we chose the clumps’ column densities to be $N_{\text{HI,cl}} = 10^{18} \text{ cm}^{-2}$ with a gas temperature of $T = 10^4 \text{ K}$ (motivated by the ‘shattering’ theory of McCourt et al. 2016), and a random velocity with each component drawn from a Gaussian distribution with standard deviation $\sigma_{\text{cl}} = 200 \text{ km s}^{-1}$. This yields a critical covering factor of $f_{c,\text{crit}} \approx 5$ (Gronke et al. 2017) which we will adopt for f_c . Furthermore, we choose the clumps’ radii to be $r_{\text{cl}} = 1 \text{ pc}$ and fix

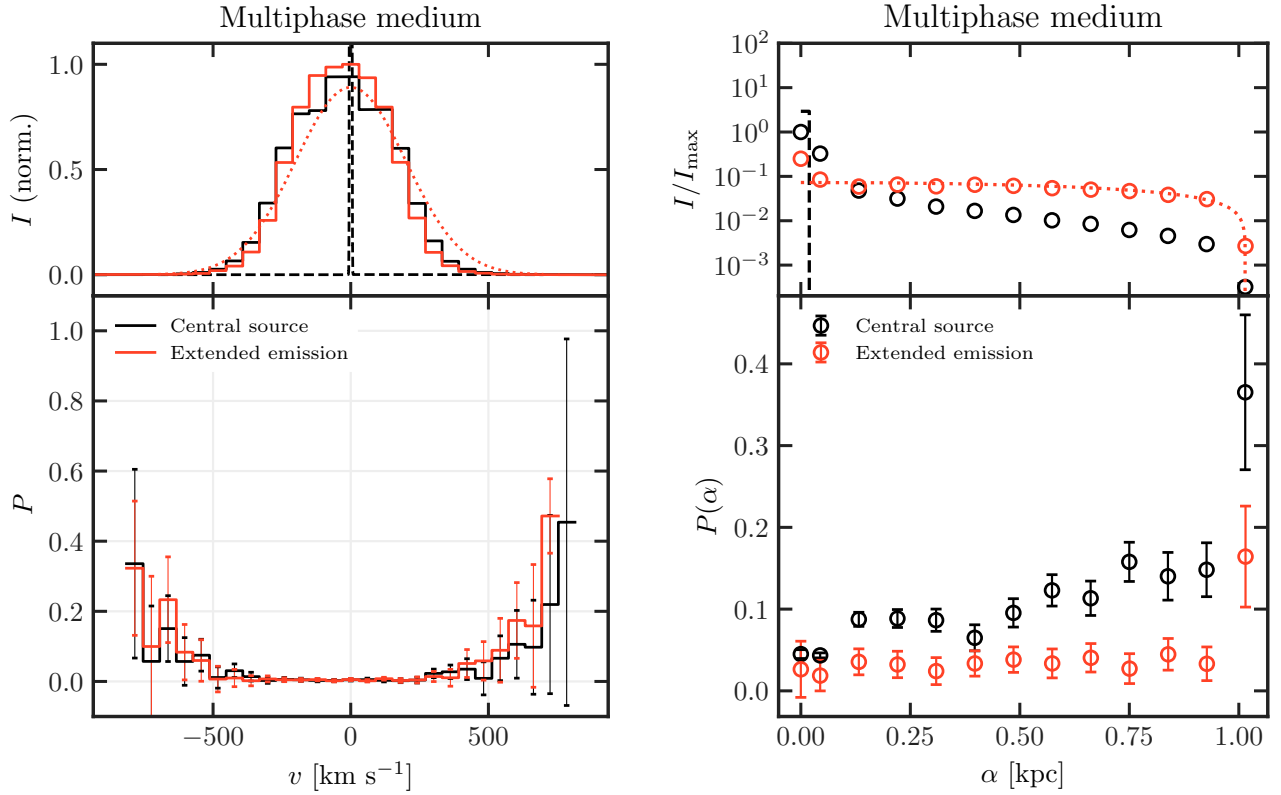


Figure 9. *Left:* Spectra of intensity and degree of polarization as function of velocity offset/frequency from Ly α line center for systems filled with many small clumps of HI gas, sized to provide a covering fraction $f_c \sim f_{c,\text{crit}}$, in an otherwise ionized medium, representative of a multiphase scattering system. We plot the emergent spectra for systems where the source of Ly α is central (black line), or where the source is extended throughout the medium (red line), ie., embedded in each cloud. Note that we do not view the sources through a slit, but rather as point sources. We also plot the intrinsic intensity spectra, the dashed black line is for the central source, and the red dotted line is for the extended source. *Right:* Surface brightness (normalized and rescaled to the maximum value obtained in the two models) and polarization profiles as function of impact parameter α for a central (black) and extend (red) source of Ly α emission in a clumpy, multiphase medium. We also plot the intrinsic surface brightness profiles, the dashed black line is for the central source, and the red dotted line is for the extended source.

the radius of the (spherical) system to 1 kpc. We note, however, that these parameters (given the others are fixed) do not influence the radiative transfer process (Hansen & Oh 2006). We set the intrinsic spectrum to have $\sigma_i = 12.85 \text{ km s}^{-1}$ (in the reference frame of the emitting gas) which corresponds to the thermal velocity of the gas.

The upper left panel of Figure 9 shows the spectra from a multiphase medium where Ly α is emitted either (a) by a central source or (b) extendedly, throughout the medium by sources residing in each clump. This is particularly visible in the intrinsic spectra, plotted with dashed and dotted lines. When having a central source, the photons are emitted close to the line center. With the extended source, the motion of the clumps must also be accounted for. Both spectra are broad, and single peaked, which is characteristic of media with $f_c \sim f_{c,\text{crit}}$ (see Figure 3 of Gronke et al. 2017). Both models also predict a degree of spatially averaged polarization which is consistent with zero over most frequencies. This is a direct consequence of our symmetric scattering geometry—even if there exist patches that are tangentially

polarized to the center, the overall geometry would cancel the global signal out, as illustrated in Figure 2. The apparent rise in polarization toward the far wings occurs at frequencies with near zero intensity.

In the right panel of Figure 9, we plot the normalized surface brightness profiles (which we after normalization render unitless by dividing with I_{\max} , the maximum surface brightness of the model with a central source) and polarization profiles of the sources as function of impact parameter α in kpc, in agreement with previous studies (see Dijkstra et al. 2006). We also plot the intrinsic, unscattered surface brightness profiles with dotted/dashed lines. In addition, the degree of polarization also differs. For the central source, P rises to $\sim 10\%$ at ~ 0.1 kpc, before it eventually rises to $\sim 15\%$. For extended sources of Ly α emission, the polarization is consistent with $P < 5\%$ out to the most distant impact parameters. The degree of polarization is lower than that obtained for scattering off clumps at low $f_c < 1$ and greater $N_{\text{HI,cl}}$ in Dijkstra & Kramer (2012), where photons that scattered only once in a clumpy outflow would produce a spatial polariza-

Table 1. Polarization through single scatterings.

Init. polarization	Core		Wing	
	90°	0/180°	90°	0/180°
Unpolarized ^a	43%	0%	100%	<i>unchanged</i>
Polarized ^b	43%	60%	100%	

NOTE—Core scattering in this regard includes only the anisotropic K transition, and not the depolarizing H transition.

^aAn initially unpolarized photon has $P = 0\%$.

^bAn initially polarized photon conversely has $P = 100\%$.

tion signal up to $P \approx 60\%$ at large impact radii. As we have a higher number of clumps along the line-of-sight (thereby a higher total optical depth) and a lower clump optical depth, the photons scatter several times per clump which reduces their polarization. This explains the lower P we obtain in the case of a central source as compared to [Dijkstra & Kramer \(2012\)](#). However, we still obtain a similar increase in P with impact radii as in other models with a central source since the radiation field is anisotropic, being stronger in the direction of the source, and the photons that escape at large radii must do so by scattering increasingly more at 90°.

This means, even though the exact degree of polarization depends on other parameters such as $N_{\text{HI,cl}}$ and the clump placement, the central source shows a rising $P(r)$ signal – while the “fluorescent” clumps, i.e., the extended source does not. This is a clear observational signal for the distinction of different $\text{Ly}\alpha$ powering mechanism, and we will explore this further in future work.

4. DISCUSSION

In this section, we discuss the origins of polarization, from quantum mechanical (§ 4.1) to astrophysical scales (§ 4.2). We discuss how $\text{Ly}\alpha$ polarization can break degeneracies between models for spectra and/or surface brightness profiles, when used *in concert* with these other observables (§ 4.3).

4.1. Polarization: the Quantum Mechanical Origins

For classical electron-scattering - which applies to $\text{Ly}\alpha$ wing scattering - unpolarized radiation that scatters at right angles become maximally polarized. In addition, the polarization properties of a single photon impose restrictions on the scattering angles: the photon cannot scatter in the direction in which it is fully polarized. For core scattering however, the ‘shape’ of quantum-mechanical wavefunctions plays a role. Unpolarized radiation still obtains the highest degree of polarization when scattering at right angles, but

only up to $P = 43\%$ via K scatterings (i.e. through the $2\text{P}_{3/2}$ state). For H scatterings (i.e. through the $2\text{P}_{1/2}$ state) polarization is only destroyed as the wavefunction of the $2\text{P}_{1/2}$ is spherically symmetric. For fully polarized radiation, i.e. with $P = 100\%$, a photon that is H scattered will only obtain $P = 43\%$ for scattering at right angles, but for forward or backward scatterings, the degree of polarization can increase to $P = 60\%$. This effect is known as *depolarization*: a photon can only obtain $P = 100\%$ through wing scatterings, and if it is scattered through the core, it will only retain, at best, $P = 60\%$. Depolarization is not possible through wing scatterings: a partially polarized photon that is forward or backward scattered will retain its polarization, or have it boosted when scattering at inclined angles.

We obtain these polarization magnitudes by using the desired scattering angles for the density matrices of the various transitions. These values agree perfectly with the results for Rayleigh or core scatterings as described, e.g., in [Chandrasekhar \(1960\)](#) or [Dijkstra & Loeb \(2008\)](#). We summarize this discussion in Table 1 which provides an overview of the polarization obtained through single scattering.

4.2. Polarization: the Astrophysical Origins

There is a difference between the probability of measuring the polarization state of an individual photon—which we just have shown can grow to prefer highly polarized photons after multiple scatterings—and observationally detecting polarization. The observable Stokes parameters describes the polarization properties of an *ensemble* of photons. While individual photons may obtain high levels of linear polarization through scattering, the ensemble averaged polarization can still be zero – if their polarization angles are not well aligned.

There are two main mechanisms behind the alignment of the polarization vectors, and thus, of generation of observable polarization: *natural asymmetries in the scattering geometry*, or *introduced asymmetries* from e.g. finite slit widths in spectropolarimeters, foregrounds or instrumental artefacts. We discuss these next.

I. Natural asymmetries: On scales where the properties of the scattering medium appears constant (local scales), any process that induces some preference in scattering direction, also introduces a preferential polarization direction. The polarization can not be oriented in the direction the photon had before scattering and it must also be perpendicular to the post-scattering propagation direction. Such a process can be an alignment of the atoms in the medium either from an external magnetic field or pumped by scatterings (see e.g. [Zhang & Yan 2018](#)), or as in our cases, an anisotropic radiation field, as also realized by [Dijkstra & Loeb \(2008\)](#). A small, local patch of the scattering medium is in general unevenly

illuminated, with strongest illumination in the direction of the source. This is the origin of the tangential polarization patterns one would obtain from scatterings in the expanding IGM (Rybicki & Loeb 1999), in spherical shells (Dijkstra & Loeb 2008), or in any of the symmetric regions of our scattering models including the spherical ellipsoid ($\varepsilon = 1/1$) in § 3.1, the centrally illuminated clumpy medium in § 3.4 with radial polarization profile given in Figure 8 or the IGM (radial profile in Figure 12). Observationally, such a polarization pattern of concentric circles was observed in LAB1 by Hayes et al. (2011), illustrated in Bower (2011). At larger impact radii, these models possess a larger degree of polarization. This is due to the larger fraction of photons escaping at right angles with increasing impact parameter. As was shown in the previous section (also see Table 1), this is accompanied by higher degrees of polarization. However, when the systems are symmetrical, their net polarization will cancel out, as illustrated in the lower row of panel a) in Figure 2.

This brings us to our next important realization: on a macroscopic, global level, scattering through a geometrically *asymmetric* system can result in polarization, as also found by Angel (1969) and Lee & Ahn (1998). This polarization is detectable even *without* spatially resolving the system. We have shown this by introducing ellipticity, biconical outflows and central disk-like obscuration. In panels b), c) and d) of Figure 2, we display examples of such asymmetric systems and their overall polarization signatures. A spatially-averaged polarization signal requires, in the first place, that the local radiation field is polarized. The global polarization orientation is then tangential to the source and reflects the location of the asymmetric regions that provide the surplus of polarized photons. For example, in the bipolar outflow, they emerge from the cones, and the polarization direction is consequently perpendicular to the outflow direction (see § 3.3). This is similar to the observations of the Egg nebula by You et al. (2017). When the local radiation fields were isotropized by a high number of core scatterings, we found, as Lee (1994) and Dijkstra & Loeb (2008) that this reduces the emergent polarization. An example of this is an outflowing, oblate system, in which an increased column density could reduce the polarization as well as flip the polarization vector (see Figure 5b). The same effect occurs in the multiphase systems studied (§ 3.4), i.e., several core scatterings lead to a decrease in polarization – as also identified by Dijkstra & Loeb (2008) in the context of intergalactic propagation.

The above asymmetries are purely *geometrical*. It is also possible to introduce asymmetries in *velocity space* since a velocity field can lower the (frequency dependent) optical depth of a system – with similar effects as described above. Examples are the ellipsoids presented in § 3.1 that became stronger polarized in the presence of global outflows, and the outflows in the biconical structures in § 3.3 which allowed

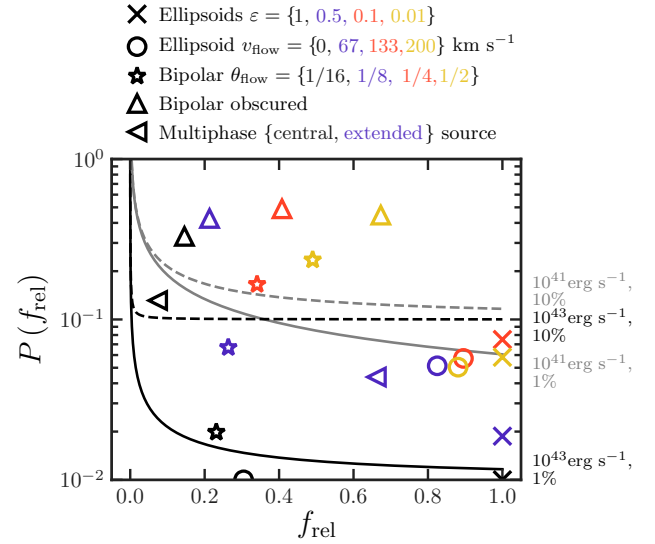


Figure 10. Detectability of models studied in this work. We show the degree of polarization at those frequencies/radii where P differs among them (with f_{rel} giving the fraction of the total flux for these, see § 4.3). The solid and dashed lines show the 1σ detection limit for a $z \sim 3$ source observed for 1 hour with a VLT-like telescope. We show the impact of a 1% (10%) systemic error, and a different luminosity, both shown as labels on the right-hand side of the plot.

for scattering in them.

II. Introduced asymmetries: These occur when observing a patch of a larger geometry (intentionally or unintentionally), that is, by effectively masking out regions which would alter the observable. This is illustrated by the sketch in Figure 2a. With a slit or aperture covering the entire system, one would detect no polarization as the symmetric polarization vectors cancel out (illustrated in the *lower panel*). However, if we observed part of the system through a narrow slit, then polarization contributions outside the slit are removed, which breaks the symmetry, and yields a surplus of polarization perpendicular to the slit alignment direction. This would result in a global (but possibly misleading) polarization signal. Of course, these issues are less important in imaging polarimetry when one can obtain Stokes parameters in a per-pixel basis (as in Hayes et al. 2011, Prescott et al. 2011 and You et al. 2017).

4.3. Polarization: Breaking Degeneracies

We have shown in the results that polarization signals themselves can be degenerate, i.e., several setups can produce similar polarization signatures. A prime example of this is the global polarization signals obtained from non-static asymmetric scattering geometries (our ellipsoids, see Figure 5b). Here, the polarization angle *flips* from being perpendicular to the major axes of the system, to being parallel to

it, when the column density is increased. Also, when further thinning the medium by introducing outflows, the degree of polarization *decreases* at higher column densities, compared to an *increase* with lower column densities.

The origins of this flip is the change of apparent geometry in different column densities (the transition from column b to c in Figure 2), by lowering the optical depth, one also transitions from escape and scattering mainly along the minor axis to scattering and escaping in the full system. In the latter case, a surplus of photons escape from the extended lobes, being polarized tangentially to the source, and perpendicular to the major axes.

Without knowledge of the apparent geometry of a system (which is generally the case), we cannot solely use the degree and direction of polarization to constrain the major axis of the system (compare the case $N_{\text{HI}}^{(c)} = 10^{19} \text{ cm}^{-2}$ and $v_{\text{exp}} = 0 \text{ km s}^{-1}$ to that of rotated system with $N_{\text{HI}}^{(c)} = 10^{21} \text{ cm}^{-2}$ and $v_{\text{exp}} = 200 \text{ km s}^{-1}$ in Figure 5b). Similarly, we cannot differentiate between a strong bipolar flow-like geometry in which the polarization arises due to scattering in lobes, and a more compact - slightly asymmetric - system with obscuration of the core (our § 3.1 compared to § 3.3): In both cases, we would have a polarization signal aligned with the major axis of the system.

However, similar degeneracies also exist when using *other observables*: The spectrum is most sensitive to the properties of the scattering medium along the path of least resistance. The ellipsoids explored in § 3.1 and § 3.2 show examples of this: the spectra do not change when the system changes from being viewed face-on to edge-on. In addition, $\text{Ly}\alpha$ spectra do not necessarily reveal intrinsic dynamics of the scattering gas. Scattering through outflows gives rise to asymmetric spectra, often with a negligible blue peak as in Figure 5a and 8. In the same figures, and in Figure 4a, we have plotted vertical dashed gray lines, which mark the range of frequencies which could be suppressed by scattering in the intergalactic medium (Dijkstra et al. 2007; Laursen et al. 2011), and leave a spectral signature virtually identical to that generated by scattering through an optically thick, outflowing medium. This illustrates that degeneracies can exist when using spectra alone.

A joint analysis of $\text{Ly}\alpha$ observables can break the mentioned degeneracies: the spectrum can constrain the column density of the optically thinner minor axis. We can then use polarization to constrain the orientation of the system. This allows, for instance, to differentiate between the polarization signals from static, asymmetric systems to those of dynamic, possibly geometrically symmetrical, systems. In static gas geometries, scattering gives rise to symmetric spectra, whereas scattering through dynamic gas geometries generally gives rise to asymmetries in the spectra. Another example relates to which processes remove flux blueward of a

galaxies systemic velocity in $\text{Ly}\alpha$ spectra: IGM or outflows. The IGM can transform an intrinsically double peaked profile emerging from a static medium into a spectrum with a dominant red peak, and can therefore mimic the effect of scattering through a galactic outflow. However, with only outflows, the polarization increases with offset from the line center (as seen in Figures 5a and 8) while it does not in static systems (see Figure 4a). A static system with the IGM processing away the blue peak would hence give rise to different polarization signature. In the case of *both* IGM processing and outflows, the *degree* of polarization can be attempted reconciled with the observed spectral shape.

Finally, in Figure 10 we quantify the ability of present-day telescopes to differentiate between polarization signatures of all our explored models. In order to do this, we define the fraction of the total flux f_{rel} where the polarization signal differs. This fraction can be defined spatially (e.g., only photons arriving in the outer regions for the multiphase media in § 3.4) or in frequency space. This corresponds to an optimally designed experiment where, for instance, the slit position has been chosen so that only photons with a positive net polarization are recorded. Specifically, we then show the degree of polarization for this fraction of photons $P(f_{\text{rel}})$ versus f_{rel} in Figure 10.

For the outflowing ellipsoids and bipolar outflows (unobscured and obscured), f_{rel} is obtained for $v > 160 \text{ km s}^{-1}$ (also indicated by vertical dashed gray lines in the spectra in Figures 5a and 8), where the polarization differ the most. For the static ellipsoids, the polarization differ similarly across the spectrum, and all frequencies are included, hence $f_{\text{rel}} = 1$ for those. We used photons arriving from $r > 0.1R_{\text{max}}$ for the multiphase media with either a central source of $\text{Ly}\alpha$ or sources extending throughout the medium as the frequency-dependent polarization for both those models were near zero. With the solid lines, we show the sensitivity¹⁵ of FORS2 at VLT. We see that it would be able to differentiate between most models if these were $L = 10^{43} \text{ erg s}^{-1}$, or even $L = 10^{41} \text{ erg s}^{-1}$, $\text{Ly}\alpha$ emitters at $z = 3$ that were observed for one hour. Separating models becomes harder if one assumes that the systemic error of the instrument is as high as 10%, except for those models where $P(f_{\text{rel}}) > 20\%$. Detecting, differentiating P and breaking the otherwise degenerate models we have explored is thus viable already today.

5. SUMMARY AND CONCLUSIONS

¹⁵ We restrict ourselves to a shot-noise/systemic-limited approximation $\sigma_P = \sqrt{1/((N_{\text{HWP}}/2)\text{SNR})^2 + \sigma_{\text{sys}}^2}$ where $N_{\text{HWP}} = 4$ is the number of half-wave plate rotations, $\text{SNR} = \sqrt{N_{\text{phot}}}$ is the signal-to-noise ratio given in the case of shot-noise only from the number of photons N_{phot} arriving at the sensor, and σ_{sys} is a systemic error. Based on Patat & Romaniello (2006).

Table 2. Intensity and polarization properties of Ly α systems explored in this paper.

	§ 3.1 Ellipsoid ^a		§ 3.2 Ellipsoidal outflow ^a		§ 3.3 Bipolar outflow ^a		§ 3.4 Multiphase medium ^b	
	Spherical	Ellipsoidal	Low v_{flow}	High v_{flow}	Small θ_{flow}	Large θ_{flow}	Central source	Extended source
$I(v)$	Symmetric double-peaked		Redshifted single-peaked		Redshifted double-peaked		Broad, single peak	
$\langle P \rangle^1$	Zero ²	~ 5%	Depends on N_{HI}		1%	10%	Zero ²	< 5% also locally
$P(v)$	Flat, nil	Flat, non-zero	Rises ³ to ~ 30%		Flat, low	Rises up to 60%	Flat, zero	
$P(r)$	Rising		Rising		Rising		Rising	Flat, zero
Figures	4a, 4b		5a, 5b		6, 7, 8		9	

NOTE—The exact numerical values are model dependent.

^aViewed edge-on.

^bOur clumpy clouds have a covering fraction close to the critical value, $f_c \sim f_{c,\text{crit}}$. Other f_c produce different spectra.

¹The global, frequency- and spatially-integrated polarization values are given as the extremes obtained for the models.

²The polarization is *locally* non-zero, however. Global symmetries cancel it out as illustrated in panel a) of Figure 2.

³These increases in P with v depends on the column density of the system and are here given for $N_{\text{HI}} = 10^{19} \text{ cm}^{-2}$ along the minor axes.

A major challenge in extragalactic astrophysics is to decode and reveal the properties of systems with only a limited set of observables. Interpreting observations of Ly α requires us to understand the transport of this radiation. Spectra and/or surface brightness profiles provide constraints on this scattering process, though sometimes not uniquely so. The polarization properties of Ly α provide additional constraints on the scattering process, but this has been explored much less in the literature, even though it has been demonstrated that extragalactic sources of Ly α source can reach significant degrees of polarization (both theoretically and observationally).

This motivated us to implement polarization into the Ly α radiative transfer code `tlac` of Gronke & Dijkstra (2014), providing us with the ability to do a joint analysis of emergent observables. To this aim, we used the *density matrix formalism* of Lee et al. (1994). Through a 2×2 matrix, it properly describes the probability of measuring a Ly α photon in either of its two helical spin states, as well as the linear superposition of these. The elements of this are modified through (Ly α) *core scatterings* near the line center and *wing scatterings* in the damping wing. As photons escape from an arbitrary three-dimensional HI scattering medium that contain a single or a distribution of Ly α sources, we convert the density matrix coefficients of each individual photon to observable Stokes parameters. This approach allowed us to treat polarization both on a quantum mechanical level as well on a statistical, observable level, setting this work apart from earlier works where only the latter could be achieved (as in Rybicki & Loeb 1999; Dijkstra & Loeb 2008 and Trebitsch et al. 2016).

We have explored scattering through a suite of simplified geometries with simplistic dynamics, such as static and expanding ellipsoids, biconical outflows, and multiphase (clumpy) outflows. We summarize some of their observable properties in Table 2. These idealized models help in understanding the physical origins of the polarization signal, and correspond to simplified setups for which other Ly α observables have been studied previously in the literature. We have shown how the global signal from an unresolved source, either its degree and angle of polarization, or its polarization spectrum, depends on its scattering symmetry. A symmetric system would appear to have zero polarization, just as one that either is sufficiently optically thick to isotropize the emergent radiation, or that emits Ly α extensively *throughout* itself (as in cooling systems, or in the case of recombinations/fluorescence) would have.

Introducing asymmetries in the scattering geometry, from the smallest to the largest scales, we showed how polarization is generated. The polarization is a measure of any surplus, or lack of, scattered photons at locations for which the scattering geometry is not fully symmetric. We explored ellipsoids and bipolar outflows as examples of this.

Alone, the polarization signal cannot – just as other observables – be used alone to describe the physical state of a source and its environment. We have shown that this is only possible when it is used in conjunction with other observables. As an example, we have shown that we obtain tangential polarization patterns around central sources. In asymmetric geometries, the polarization direction may be used to reveal the alignment of the system. But this only works if the intensity

spectrum of the system is known, as the polarization direction is degenerate between several geometries and dynamics.

Likewise, other observables should be used with caution. Knowing an intensity spectrum or luminosity of a source, one may misinterpret these as being intrinsic to the source, although in an asymmetric system with anisotropic $\text{Ly}\alpha$ escape, it is not necessarily so. The emergent intensity only reveals the properties of the medium along the path of least resistance. With polarization arising due to asymmetries, a global polarized $\text{Ly}\alpha$ signal of an unresolved source would be a strong indicator of possible anisotropies in the $\text{Ly}\alpha$ escape. In systems with anisotropic $\text{Ly}\alpha$ escape, it is easy to misinterpret this as a low $\text{Ly}\alpha$ (and in some cases, LyC) escape fraction. Moreover, IGM absorption manifests itself through an attenuation of the blue part of the intensity spectra of sources, but this could also be falsely mistaken to be caused by outflows, which also imprint this spectral signature. We have shown that it is possible to break this degeneracy with polarization measurements.

Currently, none of the next generation extremely large telescopes plan to include polarimeters intended for extragalactic use (see discussion in Hayes & Scarlata 2011). However, new, dedicated observations are undertaken (see e.g. Beck et al. 2016; You et al. 2017), promising a bright future. We have also shown that present-day telescopes would be able to differentiate between the polarization signals of most of the

models we have explored. We are currently exploring a realistic, multiphase medium in an upcoming paper, comparing it to recently obtained observations. Continued work is needed, both theoretically (see e.g. Chang et al. 2017), numerically and observationally, as we have shown in this paper that polarized $\text{Ly}\alpha$ can be a powerful, degeneracy-breaking probe into an otherwise secretive Universe.

We all thank B. Ciardi for helpful comments. We thank the referee for the highly constructive feedback. MBE is grateful to H.-W. Lee, S.-J. Chang, C. Scarlata, C. You and Ll.-M. Ribas along with other members of the observational and theoretical $\text{Ly}\alpha$ community (you know who you are) for rewarding discussions. MBE thanks the Institute of Theoretical Astrophysics at UiO and the Astronomy and Astrophysics Department at UCSC for their kind hospitality. MD thanks the physics department at UCSB for their kind hospitality. MH acknowledges the support of the Swedish Research Council, Vetenskapsrådet and the Swedish National Space Board (SNSB), and is Fellow of the Knut and Alice Wallenberg Foundation.

Software: `tlac` (Gronke & Dijkstra 2014), `numpy` (Van Der Walt et al. 2011), `Cython` (Behnel et al. 2011), `Matplotlib` (Hunter 2007).

REFERENCES

- Adams, T. F. 1971, *ApJ*, 168, 575
 Adams, T. F. 1972, *ApJ*, 174, 439
 Ahn, S., Lee, H., & Lee, H. M. 2002, *ApJ*, 567, 922
 Ahn, S.-H., & Lee, H.-W. 1998, preprint
 —. 2015, *Journal of The Korean Astronomical Society*, 48, 195
 Ahn, S.-H., Lee, H.-W., & Lee, H. M. 2000, *JKAS*, 33, 29
 Ahn, S.-H., Lee, H.-W., & Lee, H. M. 2003, *MNRAS*, 340, 863
 Angel, J. R. P. 1969, *ApJ*, 158, 219
 Avery, L. W., & House, L. L. 1968, *ApJ*, 152, 493
 Bacon, R., Brinchmann, J., Richard, J., et al. 2015, *A&A*, 575, A75
 Beck, M., Scarlata, C., Hayes, M., Dijkstra, M., & Jones, T. J. 2016, *ApJ*, 818, 1
 Behnel, S., Bradshaw, R., Citro, C., et al. 2011, *Computing in Science and Engineering*, 13, 31
 Blandford, R. D., & Rees, M. J. 1974, *MNRAS*, 169, 395
 Bower, R. 2011, *Nature*, 476, 288
 Brasken, M., & Kyrola, E. 1998, *A&A*, 332, 732
 Cai, Z., Fan, X., Yang, Y., et al. 2017, *ApJ*, 837, 71
 Cantalupo, S., Arrigoni-Battaia, F., Prochaska, J. X., Hennawi, J. F., & Madau, P. 2014, *Nature*, 506, 63
 Cantalupo, S., Porciani, C., Lilly, S. J., & Miniati, F. 2005, *ApJ*, 628, 61
 Chandrasekhar, S. 1960, Radiative transfer
 Chang, S.-J., Lee, H.-W., & Yang, Y. 2017, *MNRAS*, 464, 5018
 Chapman, S. C., Smail, I., Windhorst, R., Muxlow, T., & Ivison, R. J. 2004, *ApJ*, 611, 732
 Dijkstra, M. 2014, *PASA*, 31, 26
 Dijkstra, M., Gronke, M., & Sobral, D. 2016, *ApJ*, 823, 74
 Dijkstra, M., Haiman, Z., & Spaans, M. 2006, *ApJ*, 649, 14
 Dijkstra, M., & Kramer, R. 2012, *MNRAS*, 424, 1672
 Dijkstra, M., Lidz, A., & Wyithe, J. S. B. 2007, *MNRAS*, 377, 1175
 Dijkstra, M., & Loeb, A. 2008, *MNRAS*, 386, 492
 Djorgovski, S., Spinrad, H., McCarthy, P., & Strauss, M. A. 1985, *ApJ*, 299, L1
 Duval, F., Östlin, G., Hayes, M., et al. 2016, *A&A*, 587, A77
 Field, G. B. 1958, *Proceedings of the IRE*, 46, 240
 Gallagher, III, J. S., & Smith, L. J. 1999, *MNRAS*, 304, 540
 Geach, J. E., Alexander, D. M., Lehmer, B. D., et al. 2009, *ApJ*, 700, 1
 Gronke, M., Bull, P., & Dijkstra, M. 2015, *ApJ*, 812, 123
 Gronke, M., & Dijkstra, M. 2014, *MNRAS*, 444, 1095
 Gronke, M., & Dijkstra, M. 2016, *ApJ*, 826, 14

- Gronke, M., Dijkstra, M., McCourt, M., & Oh, S. P. 2016, *ApJL*, 833, L26
- Gronke, M., Dijkstra, M., McCourt, M., & Peng Oh, S. 2017, *A&A*, 607, A71
- Haiman, Z., Spaans, M., & Quataert, E. 2000, *ApJL*, 537, L5
- Hansen, M., & Oh, S. P. 2006, *MNRAS*, 367, 979
- Hashimoto, T., Verhamme, A., Ouchi, M., et al. 2015, *ApJ*, 812, 157
- Hashimoto, T., Ouchi, M., Shimasaku, K., et al. 2017, *MNRAS*, 465, 1543
- Hayes, M. 2015, *PASA*, 32, e027
- Hayes, M., & Scarlata, C. 2011, in *SF2A*, ed. G. Alecian, K. Belkacem, R. Samadi, & D. Valls-Gabaud (Paris: Société Française d'Astronomie et d'Astrophysique), 5
- Hayes, M., Scarlata, C., & Siana, B. 2011, *Nature*, 476, 304
- Hayes, M., Östlin, G., Schaerer, D., et al. 2013, *ApJL*, 765, L27
- Hennawi, J. F., Prochaska, J. X., Cantalupo, S., & Arrighoni-Battaia, F. 2015, *Science*, 348, 779
- Herenz, E. C., Wisotzki, L., Roth, M., & Anders, F. 2015, *A&A*, 576, A115
- Herenz, E. C., Urrutia, T., Wisotzki, L., et al. 2017, *A&A*, 606, A12
- Hogan, C. J., & Weymann, R. J. 1987, *MNRAS*, 225, 1P
- Hu, E. M., & Cowie, L. L. 1987, *ApJ*, 317, L7
- Humphrey, A., Vernet, J., Villar-Martín, M., et al. 2013, *ApJ*, 768, L3
- Hunter, J. D. 2007, *Computing in Science and Engineering*, 9, 90
- Karman, W., Caputi, K. I., Caminha, G. B., et al. 2017, *A&A*, 599, A28
- Kim, H. J., Lee, H.-W., & Kang, S. 2007, *MNRAS*, 374, 187
- Kunth, D., Mas-Hesse, J. M., Terlevich, E., et al. 1998, *A&A*, 334, 11
- Lake, E., Zheng, Z., Cen, R., et al. 2015, *ApJ*, 806, 46
- Laursen, P. 2010, PhD thesis, University of Copenhagen
- Laursen, P., Duval, F., & Östlin, G. 2013, *ApJ*, 766, 124
- Laursen, P., Sommer-Larsen, J., & Razoumov, A. O. 2011, *ApJ*, 728, 52
- Lee, H. W. 1994, *MNRAS*, 268, 49
- Lee, H.-W. 1999, *ApJL*, 511, L13
- Lee, H.-W., & Ahn, S.-H. 1998, *ApJ*, 504, L61
- Lee, H.-W., & Blandford, R. D. 1997, *MNRAS*, 288, 19
- Lee, H.-W., Blandford, R. D., & Western, L. 1994, *MNRAS*, 267, 303
- Lee, K. W., & Lee, H.-W. 1997, *MNRAS*, 292, 573
- Loeb, A., & Rybicki, G. B. 1999, *ApJ*, 524, 527
- Lynds, C. R., & Sandage, A. R. 1963, *ApJ*, 137, 1005
- Madau, P., Meiksin, A., & Rees, M. J. 1997, *ApJ*, 475, 429
- Mas-Ribas, L., & Dijkstra, M. 2016, *ApJ*, 822, 84
- Mas-Ribas, L., Dijkstra, M., Hennawi, J. F., et al. 2017, *ApJ*, 841, 19
- McCourt, M., Oh, S. P., O'Leary, R. M., & Madigan, A.-M. 2016, ArXiv e-prints, [arXiv:1610.01164](https://arxiv.org/abs/1610.01164)
- McKee, C. F., & Ostriker, J. P. 1977, *ApJ*, 218, 148
- Mori, M., Umemura, M., & Ferrara, A. 2004, *ApJL*, 613, L97
- Neufeld, D. A. 1990, *ApJ*, 350, 216
- . 1991, *ApJ*, 370, L85
- Oesch, P. A., Brammer, G., van Dokkum, P. G., et al. 2016, *ApJ*, 819, 129
- Osterbrock, D. E. 1962, *ApJ*, 135, 195
- Ouchi, M., Harikane, Y., Shibuya, T., et al. 2018, *PASJ*, 70, S13
- Partridge, R. B., & Peebles, P. J. E. 1967, *ApJ*, 147, 868
- Patat, F., & Romaniello, M. 2006, *PASP*, 118, 146
- Pierleoni, M., Maselli, A., & Ciardi, B. 2009, *MNRAS*, 393, 872
- Planck Collaboration XVI. 2014, *A&A*, 571, A16
- Prescott, M. K. M., Smith, P. S., Schmidt, G. D., & Dey, A. 2011, *ApJ*, 730, L25
- Rybicki, G. B., & Lightman, A. P. 1979, *Radiative processes in astrophysics* (Weinheim: Wiley-VCH Verlag), 382
- Rybicki, G. B., & Loeb, A. 1999, *ApJL*, 520, L79
- Schaerer, D. 2002, *A&A*, 382, 28
- . 2003, *A&A*, 397, 527
- Schuster, A. 1879, *MNRAS*, 40, 35
- Shibuya, T., Ouchi, M., Konno, A., et al. 2018, *PASJ*, 70, S14
- Spinrad, H. 1989, in *NATO Advanced Science Institutes (ASI) Series C*, Vol. 264, NATO Advanced Science Institutes (ASI) Series C, ed. C. S. Frenk, R. S. Ellis, T. Shanks, A. R. Heavens, & J. A. Peacock, 39
- Steidel, C. C., Bogosavljević, M., Shapley, A. E., et al. 2011, *ApJ*, 736, 160
- Stenflo, J. O. 1980, *A&A*, 84, 68
- Suchkov, A. A., Balsara, D. S., Heckman, T. M., & Leitherner, C. 1994, *ApJ*, 430, 511
- Taniguchi, Y., & Shioya, Y. 2000, *ApJL*, 532, L13
- Trainor, R. F., Steidel, C. C., Strom, A. L., & Rudie, G. C. 2015, *ApJ*, 809, 89
- Trebitsch, M., Verhamme, A., Blaizot, J., & Rosdahl, J. 2016, *A&A*, 593, A122
- Van Der Walt, S., Colbert, S. C., & Varoquaux, G. 2011, *Computing in Science and Engineering*, 13, 22
- Verhamme, A., Orlitová, I., Schaerer, D., et al. 2017, *A&A*, 597, A13
- Verhamme, A., Schaerer, D., Atek, H., & Tapken, C. 2008, *A&A*, 491, 89
- Verhamme, A., Schaerer, D., & Maselli, A. 2006, *A&A*, 460, 397
- Wisotzki, L., Bacon, R., Blaizot, J., et al. 2016, *A&A*, 587, A98
- Wouthuysen, S. A. 1952, *AJ*, 57, 31
- Yang, H., Malhotra, S., Gronke, M., et al. 2017, *ApJ*, 844, 171
- You, C., Zabludoff, A., Smith, P., et al. 2017, *ApJ*, 834, 182
- Zhang, H., & Yan, H. 2018, *MNRAS*, 475, 2415
- Zheng, Z., & Miralda-Escudé, J. 2002, *ApJ*, 578, 33

Zitrin, A., Labbe, I., Belli, S., et al. 2015, [ApJL](#), 810, L12

APPENDIX

A. DENSITY MATRICES FOR Ly α TRANSITIONS

Here, we will present the elements of the 2×2 density matrices describing the probability of measuring the polarization state of a photon following scattering through the three possible Ly α transitions, following [Ahn et al. \(2002\)](#) or [Ahn & Lee \(2015\)](#).

In the following, we use the left-handed photon basis $\{\boldsymbol{\varepsilon}_1, \boldsymbol{\varepsilon}_2, \boldsymbol{\varepsilon}_3\}$ where

$$\boldsymbol{\varepsilon}_1 = (-\sin \phi, \cos \phi, 0) \quad (\text{A1})$$

$$\boldsymbol{\varepsilon}_2 = (\cos \theta \cos \phi, \cos \theta \sin \phi, -\sin \theta) \quad (\text{A2})$$

$$\boldsymbol{\varepsilon}_3 = (\sin \theta \cos \phi, \sin \theta \sin \phi, \cos \theta) \quad (\text{A3})$$

with ϕ and θ as the polar angles.

The state of a Ly α photon after scattering is determined by eight unique photon parameters: (i) the photon frequency determining whether the transition occurs in the resonance core or the damping wing and hence the transition type; (ii–iii) the two polar angles θ and ϕ uniquely specifying the photon orientation prior to scattering; (iv–v) the polar angles θ' and ϕ' following a scattering; and (vi–viii) the density matrix of the unscattered photon ρ_{phot} with unique elements $\rho_{\text{phot},11}, \rho_{\text{phot},12} = \rho_{\text{phot},21}^* = \rho_{\text{phot},21}, \rho_{\text{phot},22}$. A difference in angles is given as $\Delta\phi = \phi' - \phi$. The state of the photon after a scattering can then be represented by a new density matrix ρ'_{phot} .

For H-type resonance core scatterings, through the $2P_{1/2}$ state of HI, in which the wave-function of the hydrogen atom has no angular dependence, the photon is depolarized following a scattering event and the resulting density matrix elements are

$$\rho'_{11} = \rho'_{22} = 1/2; \quad \rho'_{12} = 0. \quad (\text{A4})$$

For K-type resonance core scatterings, through the $2P_{3/2}$ state, there is a strong angular dependence and the polarization state of the incoming photon,

$$\rho'_{11} = (5 + 3 \cos 2\Delta\phi) \rho_{11} - 6 \cos \theta \sin 2\Delta\phi \rho_{12} + [(5 - 3 \cos 2\Delta\phi) \cos^2 \theta + 2 \sin^2 \theta] \rho_{22} \quad (\text{A5})$$

$$\begin{aligned} \rho'_{12} = & 3 \sin 2\Delta\phi \cos \theta' \rho_{11} \\ & + 6 [\cos \theta \cos \theta' \cos 2\Delta\phi + \sin \theta \sin \theta' \cos \Delta\phi] \rho_{12} \\ & + 3 \cos \theta (-2 \sin \theta \sin \theta' \sin \Delta\phi - \cos \theta \cos \theta' \sin 2\Delta\phi) \rho_{22} \end{aligned} \quad (\text{A6})$$

$$\begin{aligned} \rho'_{22} = & [(5 - 3 \cos 2\Delta\phi) \cos^2 \theta' + 2 \sin^2 \theta'] \rho_{11} \\ & + [(5 + 3 \cos 2\Delta\phi) \cos^2 \theta \cos^2 \theta' + 2 \cos^2 \theta \sin^2 \theta' + 12 \cos \Delta\phi \cos \theta' \cos \theta \sin \theta \sin \theta' + 2 \cos^2 \theta' \sin^2 \theta + 8 \sin^2 \theta \sin^2 \theta'] \rho_{22} \\ & + (6 \sin 2\Delta\phi \cos \theta \cos^2 \theta' + 2 \sin \Delta\phi \cos \theta' \sin \theta \sin \theta') \rho_{12}. \end{aligned} \quad (\text{A7})$$

Whereas for wing scatterings, in which the [Stenflo \(1980\)](#)-effect effectively make the transition behave as scattering off a free electron, the resulting density matrix elements are:

$$\rho'_{11} = \cos^2 \phi \rho_{11} - \cos \theta \sin 2\Delta\phi \rho_{12} + \cos^2 \theta \sin^2 \Delta\phi \rho_{22} \quad (\text{A8})$$

$$\begin{aligned} \rho'_{12} = & 1/2 \cos \theta' 2\Delta\phi \rho_{11} \\ & + [\cos \theta \cos \theta' \cos 2\Delta\phi + \sin \theta \sin \theta' \cos \Delta\phi] \rho_{12} \\ & - \cos \theta (\sin \theta \sin \theta' \sin \Delta\phi + 1/2 \cos \theta \cos \theta' \sin 2\Delta\phi) \rho_{22} \end{aligned} \quad (\text{A9})$$

$$\begin{aligned} \rho'_{22} = & \cos^2 \theta' \sin^2 \Delta\phi \rho_{11} \\ & + \cos \theta' [2 \sin \theta \sin \theta' \sin \Delta\phi + \cos \theta \cos \theta' \sin 2\Delta\phi] \rho_{12} \\ & + (\cos \theta \cos \theta' \cos \Delta\phi + \sin \theta \sin \theta')^2 \rho_{22}. \end{aligned} \quad (\text{A10})$$

B. TRANSLATING TO AN OBSERVER-SPECIFIC COORDINATE SYSTEM

The polarization vectors $\boldsymbol{\varepsilon}_1$ and $\boldsymbol{\varepsilon}_2$ chosen by [Ahn & Lee \(2015\)](#) were specific for a semi-infinite planar slab in the x , y -directions. The density matrix elements are composed of the (possibly complex) coefficients c_1 and c_2 which were estimated for the chosen polarization vectors $\boldsymbol{\varepsilon}_1$ and $\boldsymbol{\varepsilon}_2$, which also are given in Eqs. A1 and A2.

For a more general case, it can be useful to translate these coordinate-specific coefficients to a more general geometry. Writing the polarization state vector as \mathbf{P} in terms of its components $\boldsymbol{\varepsilon}_1$ and $\boldsymbol{\varepsilon}_2$,

$$\begin{aligned} \mathbf{P} &= c_1 \boldsymbol{\varepsilon}_1 + c_2 \boldsymbol{\varepsilon}_2 = c_1 (-\sin \phi \mathbf{e}_x + \cos \phi \mathbf{e}_y) + c_2 (\cos \theta \cos \phi \mathbf{e}_x + \cos \theta \sin \phi \mathbf{e}_y - \sin \theta \mathbf{e}_z) = \\ &= (-c_1 \sin \phi + c_2 \cos \theta \cos \phi) \mathbf{e}_x + (c_1 \cos \phi + c_2 \cos \theta \sin \phi) \mathbf{e}_y - c_2 \sin \theta \mathbf{e}_z, \end{aligned} \quad (\text{B11})$$

allows us to instead express the polarization state vector \mathbf{P} in terms of the Cartesian components with related coefficients

$$c_x = -c_1 \sin \phi + c_2 \cos \theta \cos \phi \quad (\text{B12})$$

$$c_y = c_1 \cos \phi + c_2 \cos \theta \sin \phi \quad (\text{B13})$$

$$c_z = -c_2 \sin \theta. \quad (\text{B14})$$

We can now construct an observer-specific density matrix, relative to the three Cartesian unit vectors,

$$\rho_{\text{obs}} = \mathbf{P} \mathbf{P}^\dagger = \begin{pmatrix} c_x c_x^* & c_x c_y^* & c_x c_z^* \\ c_y c_x^* & c_y c_y^* & c_y c_z^* \\ c_z c_x^* & c_z c_y^* & c_z c_z^* \end{pmatrix} \quad (\text{B15})$$

which can be expressed in terms of the coefficients c_1 and c_2 ,

$$\begin{aligned} |c_x^2| &= |c_1^2| \sin^2 \phi \\ &\quad - (c_1 c_2^* + c_2 c_1^*) \sin \phi \cos \theta \cos \phi \\ &\quad + |c_2^2| \cos^2 \theta \cos^2 \phi, \end{aligned} \quad (\text{B16})$$

$$\begin{aligned} |c_y^2| &= |c_1^2| \cos^2 \phi \\ &\quad + (c_1 c_2^* + c_2 c_1^*) \cos \phi \cos \theta \sin \phi \\ &\quad + |c_2^2| \cos^2 \theta \sin^2 \phi, \end{aligned} \quad (\text{B17})$$

$$|c_z^2| = |c_2^2| \sin^2 \theta, \quad (\text{B18})$$

$$\begin{aligned} c_x c_y^* &= -|c_1^2| \sin \phi \cos \phi \\ &\quad - c_1 c_2^* \sin \phi \cos \theta \sin \phi \\ &\quad + c_2 c_1^* \cos \theta \cos^2 \phi \\ &\quad + |c_2^2| \cos^2 \theta \cos \phi \sin \phi, \end{aligned} \quad (\text{B19})$$

$$\begin{aligned} c_x c_z^* &= c_1 c_2^* \sin \phi \sin \theta \\ &\quad - c_2 \cos \theta \cos \phi \sin \theta, \end{aligned} \quad (\text{B20})$$

$$\begin{aligned} c_y c_z^* &= -c_1 c_2^* \cos \phi \sin \theta \\ &\quad - |c_2^2| \cos \theta \sin \phi \sin \theta, \end{aligned} \quad (\text{B21})$$

$$c_x^* c_y = (c_x c_y^*)^*, \quad c_x^* c_z = (c_x c_z^*)^*, \quad c_y^* c_z = (c_y c_z^*)^*, \quad (\text{B22})$$

that can be retrieved directly from the original density matrix' components,

$$|c_1^2| = \rho_{11}, \quad c_1 c_2^* = \rho_{12}, \quad c_1^* c_2 = \rho_{21}, \quad |c_2^2| = \rho_{22}, \quad (\text{B23})$$

where $\rho_{12} = \rho_{21}$ when there is no circular polarization ($V = 0$, and hence all elements are real).

C. COMPARISONS

C.1. *Semi-Infinite Slab*

To test our implementation of the density matrix formalism in `tlac`, we compare it under the same geometry that was applied by [Ahn & Lee \(2015\)](#). In [Figure 11](#) we show results for a slab that is infinitely large in the x, y directions. This orientation ensures it to be aligned with the basis chosen to represent the density matrix. The observable Stokes parameters do in this case coincide with the per-photon Stokes parameters. These can be obtained from the density matrix components, with $I = \rho_{11} + \rho_{22}$, $Q = \rho_{11} - \rho_{22}$ and $U = \rho_{12} + \rho_{21}$. We hence do not have to translate the components as in [Appendix B](#). For the semi-infinite slab, polarization may only develop either parallel to the slab normal or perpendicular to it, which corresponds to the two basis vectors. No cross-terms do then exist, and U is zero. In the figure, we then only plot Q as a function of viewing angle $\mu = \cos \theta$ to the surface, where $\mu = 1$ corresponds to viewing the slab nadir. The optical depth from the midplane of the slab is 2×10^6 , and $T = 10$ K. This corresponds to the optically thick limiting case in which the photons escape from the damping wing after having undergone a diffusion process. There, the polarization is given by the Rayleigh phase function, in which the polarization develops similarly to a process where a continuum photon is scattered by a free electron, for which [Chandrasekhar \(1960\)](#) developed a solution, overplotted in the figure. Our results fit those of [Ahn & Lee \(2015\)](#) and [Chandrasekhar \(1960\)](#) well, with larger polarization developing for sharper viewing angles ($\mu \rightarrow 0$).

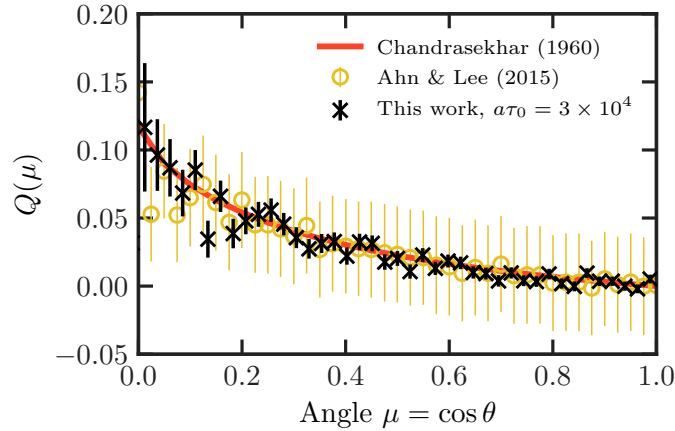


Figure 11. Degree of Q -polarization calculated in a semi-infinite plane-parallel slab of neutral hydrogen with $T = 10$ K and $\tau_0 = 2 \times 10^6$ and the similar calculations by [Ahn & Lee \(2015\)](#) who introduced the implemented density matrix formalism and an analytical solution by [Chandrasekhar \(1960\)](#) for electron scatterings in an optically thick slab, showing good agreement.

C.2. *Universe Before Reionization: Scattering Out of Resonance Due to the Hubble Expansion*

We compare our polarization implementation with that of [Rybicki & Loeb \(1999\)](#), who (also through the companion paper [Loeb & Rybicki 1999](#)) examined scattering of $\text{Ly}\alpha$ photons through neutral hydrogen in an expanding Hubble volume, representative of the high- z , pre-reionization Universe. They predicted that $\text{Ly}\alpha$ is detectable as halos with a characteristic radius of $\sim 10 - 20$ arcseconds, and redshifted by several 10^3 km s^{-1} with respect to systemic due to the Hubble flow (the precise numbers depend on cosmological parameters). [Rybicki & Loeb \(1999\)](#) computed the polarization properties of these $\text{Ly}\alpha$ halos, and found them to be highly polarized, with the degree of linear polarization reaching $\sim 60\%$. [Rybicki & Loeb \(1999\)](#) compared their results to [Schuster \(1879\)](#), where the polarization was directly related to the radial dependence of the product of the cross section and the column density. We, however, note that the degree of polarization is consistent with photons that have developed 100% polarization in an early wing scattering that then is core-scattered forward (see [Table 1](#)).

To test our polarization implementation, we repeated the analysis of [Rybicki & Loeb \(1999\)](#), and compared results. We adopted $\Omega_b = 0.06$, $\Omega_m = 0.7$ and $\Omega_\Lambda = 0.7$ and $h_0 = 0.7$, which translates to a mean present-day hydrogen number density $n_{\text{HI},0} = x_{\text{HI}} X n_b$ where $n_b = 2.5 \times 10^{-7} \text{ cm}^{-3}$ ([Planck Collaboration XVI 2014](#)), x_{HI} is the neutral hydrogen fraction, and X is the primordial number density of hydrogen, giving $n_{\text{HI}}(z) = n_{\text{HI},0} (1+z)^3$. Following [Loeb & Rybicki \(1999\)](#) and [Rybicki & Loeb \(1999\)](#) we assumed that $x_{\text{HI}} = 1$, and focused on $z = 10$. We emitted 10^7 photons centered at the $\text{Ly}\alpha$ line frequency, and set the core-skipping parameter $x_{\text{crit}} = 10$. We captured all photons escaping within 15° of the six principal axes, and binned the photons into logarithmic bins of their impact parameters. We then calculate the collective degree of linear polarization in

each bin, $P(\alpha_x, \alpha_y)$ where α_x and α_y are their two dimensional impact parameters, as well as the variance. We calculate the uncertainty following the procedure outlined in App. (D). We then computed photon weighted averages of the linear polarization, $P(\alpha)$, where α now is the radial impact parameter.

Figure 12a compares our results to those of Rybicki & Loeb (1999). We plot our normalized intensity I/I_{\max} and the degree of total linear polarization $P(\alpha)$ as function of radial impact parameter α (*open black circles* with error bars), and compare to results from Figure 1 in Rybicki & Loeb (1999), and rescale their normalized impact parameter $\tilde{\rho}$ using Eq. (9) in Loeb & Rybicki (1999) with our choice of cosmological parameters. We find our results to fit the rescaled results of Rybicki & Loeb (1999) well. We slightly underestimate $P(\alpha)$ at larger α . We attribute the discrepancies in the degree of polarization to the choice of cosmology.

C.3. Scattering in an Ionized Medium off an Expanding, Neutral Shell of Hydrogen

Dijkstra & Loeb (2008) explored the polarization of $\text{Ly}\alpha$ photons scattering through the often-used shell models. We repeat their analysis for a shell with column density $N_{\text{HI}} = 10^{19} \text{ cm}^{-2}$ at $T = 10^4 \text{ K}$, $v_{\text{outflow}} = 200 \text{ km/s}$. In this simulation, we include all core scatterings (i.e. $x_{\text{crit}} = 0$). The central $\text{Ly}\alpha$ source emits unpolarized photons with frequencies Gaussian-distributed around the $\text{Ly}\alpha$ line center, with $\sigma = v_{\text{circ}}$. Figure 12b compares the rescaled and then normalized intensity I/I_{\max} and the degree of linear polarization $P(\alpha)$. Our results are represented by the *open black circles*, whereas those of Dijkstra & Loeb (2008) are represented by the *solid, purple line*. Both results agree well.

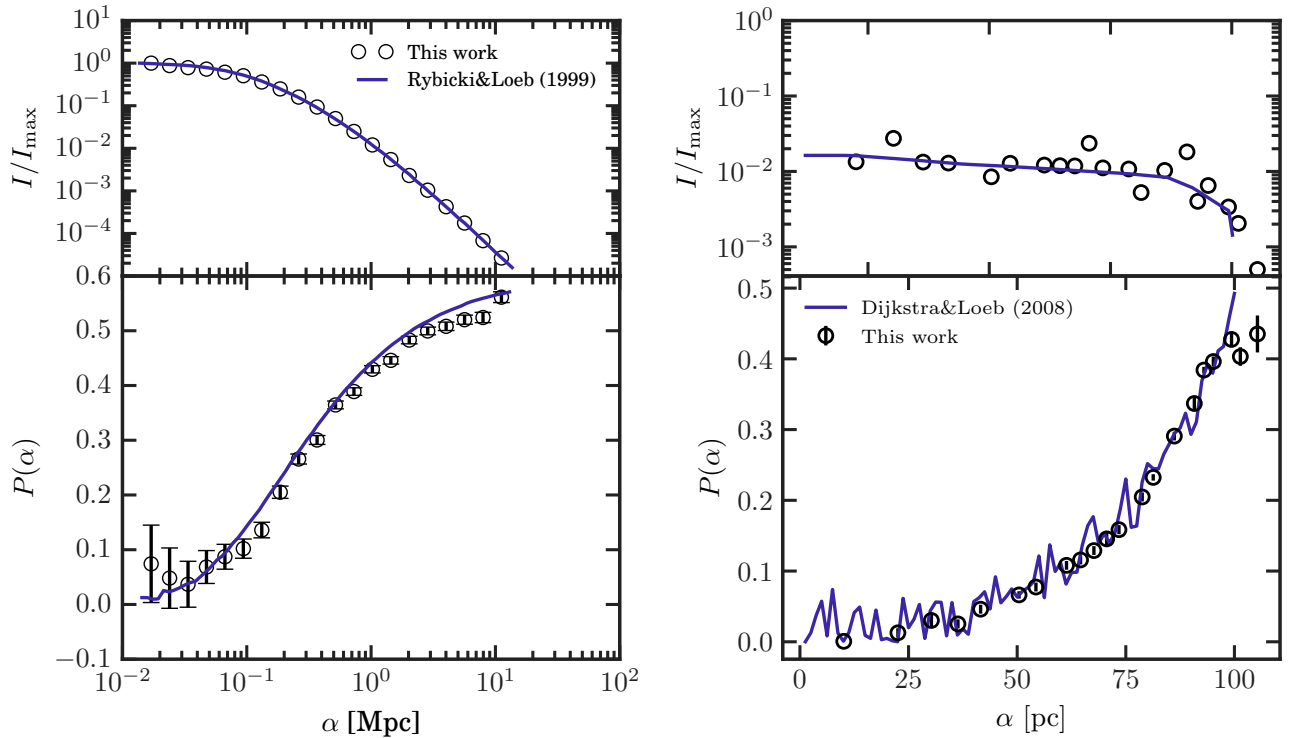


Figure 12. Upper panels: normalized intensity as function of impact parameter. Lower panels: degree of linear polarization against impact parameters. In panels (a), we compare our methods against the results of Rybicki & Loeb (1999) (solid, purple lines) for scattering in an Hubble-expanding medium of HI at $z = 10$, and in panels (b), we compare our methods (empty, black circles, with error bars for $P(\alpha)$) against the results for an expanding shell of HI by Dijkstra & Loeb (2008) (solid, purple lines).

D. ESTIMATING UNCERTAINTY

The polarization in each bin (pixel) is estimated from the contributions from all the photons falling into it. The arrival of photons on a detector is a Poissonian process, which for large number of photons is well described by Gaussian statistics. The

variance can be estimated from the accumulated (or mean) polarization P_j in a pixel j and the per-photon polarization $P_{i,j}$,

$$\sigma_j^2 = \frac{1}{N_j - 1} \sum_{i=1}^{N_j} (P_{i,j} - P_j)^2. \quad (\text{D24})$$

To calculate the polarization as a function of the radial impact parameter α , we bin the polarization in multiple pixels with (approximately) the same α ,

$$P(\alpha) = \frac{\sum_{j \in \alpha} w_j P_j}{\sum_{j \in \alpha} w_j} \quad (\text{D25})$$

where we have weighted the contributions by the number of photons going into each pixel j , N_j , and the variance σ_j^2 ,

$$w_j = \frac{N_j}{\sigma_j^2}. \quad (\text{D26})$$

We calculate the standard error of the mean polarization $P(\alpha)$ by propagating the per-pixel standard error,

$$\text{SE}(P(\alpha)) = \sqrt{\sum_{j \in \alpha} \frac{1}{N_j} \left(\frac{\partial P(\alpha)}{\partial w_j} \sigma_j \right)^2} = \frac{1}{\sum_{j \in \alpha} w_j} \sqrt{\sum_{j \in \alpha} \frac{N_j}{\sigma_j^2}}. \quad (\text{D27})$$